Probing Our Heliospheric History I: High-Resolution Observations of Na I and Ca II Along the Solar Historical Trajectory

Katherine Wyman[1,2] and Seth Redfield[2]

[1]Harvard-Smithsonian Center for Astrophysics, 60 Garden Street, Cambridge, MA 02138, USA kwyman@cfa.harvard.edu

[2]Astronomy Department, Van Vleck Observatory, Wesleyan University, Middletown, CT 06459, USA sredfield@wesleyan.edu

Received _____; accepted _____

ABSTRACT

Over the course of its motion through the Galaxy, our solar system has encountered many interstellar environments of varying characteristics. Interstellar medium (ISM) density variations spanning seven orders of magnitude are commonly seen throughout the general Galactic environment, and a sufficiently dense cloud within this range has the potential to dramatically alter the structure of the heliosphere. We present observations of the ISM environments the Sun has most recently encountered based on high-resolution optical spectra toward nearby stars in the direction of the historical solar trajectory. The data were obtained with the highest-resolution spectrographs available, including the Tull Spectrograph on the Harlan J. Smith Telescope at McDonald Observatory and the Ultra-High-Resolution Facility on the Anglo-Australian Telescope at the Anglo-Australian Observatory. Observations were made of interstellar Na I and Ca II doublet absorption toward 43 bright stars within ∼500 pc. No absorption is seen out to a distance of 120 pc (consistent with the outer boundary of the Local Bubble), but a complex collection of absorbers is seen in stars beyond 120 pc. While common absorbers are consistently seen in most sight lines, significant spatial variation is also detected, even between closely spaced sight lines. This pervasive evidence of small-scale structure not only speaks to the complexity of the morphology or physical properties of the gas in the ISM, but also emphasizes that dramatic structural changes to the heliosphere are common and it is important to understand the implications of such changes, such as the modulation in the cosmic ray flux, on planets.

Subject headings: Galaxy: local interstellar matter — ISM: clouds — ISM: structure — Line: profiles — Sun: heliosphere — Techniques: spectroscopic

1. Introduction

As stars hurtle along their orbits around the Galaxy, they pass through a diverse array of interstellar medium (ISM) environments, ranging from dense molecular clouds (e.g., molecular knots in Orion, $n \gtrsim 10^5$ cm^{-3}; O'dell 2001) to rarefied regions, heated and largely vacated by strong supernovae or stellar winds (as seems to be the case with the Local Bubble, $n \lesssim 10^{-2}$ cm^{-3}; Welsh & Shelton 2009). Such a dramatic variation in the characteristics of the local interstellar environment of stars can have a profound impact on the conditions in the volume occupied by planets. A balance of the pressures, between an outward moving stellar wind and the inward confinement of the surrounding interstellar material, defines an interface, the boundary between the star and the rest of the universe. In the case of our Sun, this interface, or heliopause, is located at approximately 300 AU (e.g., Müller et al. 2006), a direct consequence of the properties of the local interstellar medium (LISM) and the solar wind (i.e., their density and velocity).

Changes in the extent of the heliosphere occur over a multitude of time scales. In the short term, the solar wind strength fluctuates over its 22-year magnetic cycle while solar flares and coronal mass ejections can drive variability on even shorter time scales. Coronal activity has the potential to asymmetrically modify the morphology of the heliosphere. An event like this occurred in 2003 and was recorded by instruments aboard Voyager 1 (Decker et al. 2005). On longer time scales, a gradual change in the solar wind strength will occur over the 10-billion-year life span of the Sun. Observations of other solar type stars suggest that the historical solar wind may have been $\sim$50$\times$ stronger than it is today (Wood et al. 2005). However, the most dramatic driver of the structure of the heliosphere originates outside its boundaries (i.e., the properties of the surrounding ISM).

Currently the Sun is moving through a large ($R \sim 100$ pc), hot ($T \sim 10^6$ K), and low density ($n \sim 0.005$ cm^{-3}) cavity known as the Local Bubble. Found within the

Local Bubble are a collection of smaller (1–10 pc), higher density ($n \sim 0.1$ cm^{-3}), cooler ($T \sim 7000$ K), partially ionized clouds (Redfield & Linsky 2008). Given current solar velocity measurements (e.g., Dehnen & Binney 1998), a cloud 1 pc in diameter would pass over the solar system in just 70,000 years. Currently, the Sun resides very near to the inside edge of one of these clouds referred to as the Local Interstellar Cloud (LIC). Given the relative velocity vectors of the Sun and the LIC, the Sun will be transitioning out of the LIC sometime in the next few thousand years (Redfield & Linsky 2000). In fact, the farthest Oort Cloud objects might have already breached this boundary and moved into hot Local Bubble material. The Local Bubble is also home to clouds of much higher densities and cooler temperatures. The Local Leo Cold Cloud, a thin cloud first identified in H I 21 cm emission has recently been identified to be located between 11.3 and 24.3 pc away (Meyer et al. 2006; Peek et al. 2011). This cloud appears to have a temperature of $\sim$20 K and a H I density of $\sim$3000 cm^{-3} (Meyer et al. 2012). In addition, several of the MBM clouds (Magnani et al. 1985), originally identified by 2.6 mm CO emission, may be at or within the Local Bubble boundary. In particular, in roughly the same direction as the survey presented here, high-resolution observations of nearby stars were used to pinpoint the distance of MBM 20 (Penprase 1993; Hearty et al. 2000). A comprehensive review of the LISM is provided by Frisch et al. (2011).

Given the pliable nature of the heliosphere and the configuration of our local galactic environment, several questions arise: How will the heliosphere respond when the Sun exits the LIC? What would happen if the Sun were to traverse a dense interstellar cloud, such as the Local Leo Cold Cloud? The current paper develops the foundation for such an investigation by asking: What were the interstellar environments of the Sun in its most recent past?

The implications of a dynamic heliosphere go well beyond structural changes and could

be important for planets and their atmospheres. The relationship between our interstellar environment and the Earth has interested researchers for almost a century. Shapley (1921) first formally suggested a link between the passage of the solar system through dense ISM clouds and quasi-periodic climate catastrophes and mass extinctions of organisms on Earth. As a testament to its broad appeal, theoretical speculations on this relationship have continued to this day (Hoyle & Lyttleton 1939; Fahr 1968; Begelman & Rees 1976; Talbot et al. 1976; Frisch & York 1986; Thaddeus 1986; Zank & Frisch 1999; Shaviv 2003). A recent compendium of articles related to the solar journey through the Galaxy is given in Frisch (2006). Mechanisms invoked to link the ISM and planetary atmospheres include: (1) fluctuations of cosmic ray flux modulated through the heliosphere, given that the solar magnetic field extends only as far as the termination shock (e.g., Giacalone & Jokipii 1999; Usoskin et al. 2005; Smith & Scalo 2009); and (2) dust accretion directly onto planetary atmospheres (e.g., Pavlov et al. 2005). These processes have potential consequences for climate, ozone chemistry, and DNA mutation rates for surface organisms (see review by Scherer et al. 2006).

This work builds on a legacy of high-resolution ISM observations in the optical. The strength of the Na I and Ca II transitions has made them invaluable tracers of the ISM, even when they are trace ions in interstellar gas (as is the case in the LISM, where for example, Ca III is the dominant form of calcium and Na II is the dominant form of sodium; Slavin & Frisch 2008). Surveys have been made along sight lines toward most of the bright stars across the entire sky (Vallerga et al. 1993; Welty et al. 1994, 1996), of star-forming regions (e.g., Orion; Frisch et al. 1990; Welsh et al. 2005), and of wide binaries used to search for small-scale structure in the ISM along almost identical sight lines (e.g., Meyer & Blades 1996). However, as far as we know, this is the densest high-resolution absorption line survey of any particular direction through the ISM. Not only is this particular sight line of interest to understand the history of solar interactions with the

surrounding interstellar gas, but also this survey provides a detailed and densely sampled look at the physical properties of the galactic ISM.

A companion paper (Wyman & Redfield 2013, hereafter Paper II) explores the potential consequences an encounter with the ISM environments presented in this paper could have on the solar system. Models of the heliosphere have been made to explore a wide range of different interstellar environments by Müller et al. (2006). In particular, models were made using characteristics of the clouds in the LISM, as well as the hot Local Bubble and cold dense molecular clouds. These models provide relations between the interstellar properties and heliospheric properties. Here, we present observations of the interstellar clouds traversed by the Sun and plan to use these relationships to make estimates of the historical heliospheric response (and thereby the cosmic ray flux history on the Earth's atmosphere) in our companion paper. We defer additional discussion to Paper II, including the likelihood that the current interstellar column in the direction of the historical solar motion is identical with that of the actual interstellar environments traversed by the Sun over that time. In this paper, we focus primarily on presenting the rich dataset and providing an analysis of the ISM in this unique direction.

2. Observations

Stars were observed to measure ISM absorption in the direction of the Sun's path through the Galaxy, out to a distance of ∼500 pc. The direction and velocity of the solar peculiar velocity were derived from Dehnen & Binney (1998), who measure the solar peculiar velocity from the *Hipparcos* dataset (see Schönrich et al. 2010 for an alternative analysis). The adopted values are $l_0 = 207.70°$ and $b_0 = -32.41°$, in the constellation Eridanus. The magnitude of the solar peculiar velocity is estimated to be 13.38 ± 0.42 km s^{-1}, which corresponds to a time of ∼36.7 million years to traverse 500 pc. This represents less than 1%

of the total path length the Sun traverses in a single orbit around the Galaxy. This small percentage allows us to approximate the Sun's recent historical trajectory as a straight line toward l_0, b_0.

Stars for this study were chosen based on a close proximity ($\theta < 10°$) to l_0, b_0, and properties that optimize ISM absorption analysis (e.g., bright [$V < 8$], rapidly rotating, early type [B, A, F] stars). We use the revised *Hipparcos* parallaxes presented by van Leeuwen (2007) to calculate distances to our target stars, and restricted our sample to targets for which the relative error in distance is $\leq$0.5, whereas the median relative error is $\leq$0.1. This restriction led us to remove three targets (HD30020, HD29173, and HD30076).

We observed two targets (HD26574, 37.31 pc; HD26994, 289 pc) that were more than 9 degrees from the direction of the historical solar trajectory. HD26574, the closer target showed no interstellar absorption, while HD26994 had absorption that was dramatically different from what was observed for the rest of our sample. For this reason, we decided to constrain our sample cone to <9° from the solar historical trajectory. A third target, HD32964 (66 Eri), is a well-known short period binary ($P = 5.5$ days; Makaganiuk et al. 2011) in which both stars displayed stellar absorption features at velocities at which we would expect to see LISM absorption. Because this target is only 94.7 pc away, and given the results from our entire sample, we would not expect to see any interstellar absorption since the closest target with detected absorption is 125.9 pc and 112.9 pc for Ca II and Na I, respectively. Therefore, we removed these targets from our sample. The remaining 43 targets are listed in Table 1 and their distribution on the sky is illustrated in Figure 1.

Data were obtained throughout the time period of October 2003 through October 2005. Absorption lines of neutral sodium (Na I D_1 and D_2; 5895.9242 and 5889.9510 Å) and singly ionized calcium (Ca II H and K; 3968.4673 and 3933.6614 Å) were chosen as the ISM component tracers since they both have strong doublet resonance lines in the

optical that are sensitive to nearby interstellar clouds. Observations were made with the highest-resolution spectrographs available in each hemisphere. In the northern hemisphere, observations were taken with the Harlan J. Smith Telescope (HJST), a 2.7 meter telescope located at McDonald Observatory in west Texas. Observations were made at three separate resolution ($R \equiv \frac{\lambda}{\Delta\lambda}$) settings: TS12: Tull Spectrograph ($R \sim$ 400,000; Tull 1972), TS21: Cross-Dispersed Echelle Spectrograph (2d coudé) focus 1 ($R \sim$ 240,000; Tull et al. 1995), and TS23: Cross-Dispersed Echelle Spectrograph (2d coudé) focus 3 ($R \sim$ 60,000; Tull et al. 1995). In the southern hemisphere, observations were taken with the 3.9 meter Anglo-Australian Telescope (AAT), located at the Anglo-Australian Observatory in Australia. Spectra were obtained with the Ultra-High-Resolution Facility (UHRF), an echelle spectrograph located at the coudé focus ($R \sim$ 940,000; Diego et al. 1995). A subset of targets were observed multiple times at different resolutions and with both facilities to provide consistency checks on measurements of absorption profile parameters (see Section 2.3 for a discussion of sight lines observed with multiple configurations).

Table 2 lists the observational parameters for all data included in this study and is ordered by distance from the Sun. The approximate continuum signal-to-noise (S/N) ratio is given for each observation, as is the projected radial velocity of Earth's atmosphere at the time of the observation. Telluric features, both water vapor and sodium, can contaminate this spectral region, and are easily identified by their radial velocity.

2.1. Data Reduction

The data were reduced using Image Reduction and Analysis Facility (IRAF; Tody 1993) and Interactive Data Language (IDL) routines to subtract the bias, flat-field the images, remove scattered light and cosmic-ray contamination, extract the echelle orders, calibrate the wavelength solution, and convert to heliocentric velocities. Wavelength

calibration images were taken using a Th-Ar hollow cathode before and after each target.

The sodium region of the spectrum suffers from weak, but pervasive, telluric contamination from water in Earth's atmosphere that must be identified and removed from the data, particularly for observations toward nearby stars that may be expected to exhibit weak interstellar absorption. A forward modeling technique demonstrated by Lallement et al. (1993) was used to remove telluric line contamination in the vicinity of the Na I D lines based on a terrestrial atmosphere model (the Atmospheric Transmission [AT] program, from Airhead Software, Boulder, Colorado) developed by E. Grossman. Figure 2 shows a typical observed spectrum along with a fit to the telluric contamination. Given that scores of telluric lines are involved in the fit, the telluric model is tightly constrained and highly successful at removing the water vapor contamination from our spectra. Note that telluric lines are relatively absent in the vicinity of the Na I D_1 line at 5895.9242 Å, which further reduces any systematic influence of telluric features on the ISM profile fit. Observing both transitions of the Na I doublet is an important confirmation that the telluric subtraction is successful. With two independent measurements of Na I absorption at the same projected velocity, it is easy to identify contaminating telluric lines. Broad features remaining in the spectrum after telluric absorption removal are typically stellar absorption, which can be confirmed given the known stellar radial velocity and removed with a low-order polynomial to reveal the ISM absorption.

2.2. Spectral Analysis

All absorption profiles were fit using standard methods (see Linsky & Wood 1996; Redfield & Linsky 2002). This involves estimating the stellar continuum, determining the fewest absorption components required to obtain a satisfactory fit, convolving the absorption feature with an instrumental line-spread function, and fitting all lines of the

same ion simultaneously. Determining the stellar continuum is usually straightforward when one is dealing with high-resolution data, and systematic errors in this procedure are further reduced when multiple resonance lines of the same ion are fit simultaneously. Figure 2 shows an example of a stellar continuum that is typically encountered. The continuum is slowly varying across the narrow wavelength range and easily fit with a low ($\lesssim$5) order polynomial. Voigt absorption profiles are fit to Na I and Ca II lines simultaneously using atomic data from Morton (2003). While the continuum is not fit simultaneously with the ISM profile, in rare cases, the simultaneous ISM profile fits highlighted discrepancies between the two transitions that could be resolved with a better continuum model. In these cases, an iterative approach to the continuum modeling was used. Best-fit parameters are derived using a Marquardt χ^2 minimization technique (Press et al. 2002). Each sight line was initially fit with one component unless visual inspection of the spectrum strongly suggested the presence of multiple components. Additional components were added until an F-test (Bevington 2003) indicated that their inclusion was no longer statistically warranted. The final model spectrum is a convolution between these intrinsic Voigt profiles and the instrumental line spread function. The final fit parameters for each absorber are the central velocity (v), the line width or Doppler parameter (b), and the column density (N) along the line of sight. Errors on the fit parameters were derived from Monte Carlo simulations of the simultaneous fit. In order to evaluate the contribution of systematic errors we compare our fit errors with the standard deviation of fit parameters of the two transitions fit independently and the simultaneous fit, and use the larger of the two. Table 3 lists the final fit parameters for all individual Ca II absorbers, while Table 4 gives the total column density along each sight line. Tables 5 and 6 are the same for the Na I observations.

Figures 3a through 3o are the flux-normalized, best-fit results of the fitting process in the heliocentric rest frame, for each sight line in the sample with detected interstellar absorption, ordered by distance to each background star. Absorption spectra for each line

in both sodium and calcium doublets are shown, as well as each individual absorption component prior to convolution with the line-spread function. The hyperfine structure of Na I is modeled, but only impacts the fits of observations taken at the highest spectral resolution (Welty et al. 1994). The fit to the total absorption profile is plotted after convolution with the instrumental line-spread function.

2.3. Multiple-Resolution Observations

Our data set contains nine sight lines along which the ISM absorption was measured multiple times at different resolving powers (see Table 7). In almost all cases, the highest-resolution observation was chosen to represent the ISM absorption along the line of sight. Figure 2 shows an example of ISM absorption toward the star HD28497 observed at different spectral resolution. Spectra obtained at high resolution (TS21; $R \sim 240,000 = 1.3$ km s^{-1}) resulted in a 10 component fit, validated by the F-test, while lower-resolution data (TS23; $R \sim 60,000 = 5$ km s^{-1}) led to a fit consisting of only 6 components. However, the total column densities were essentially identical (within $\sim 0.3\sigma$), where the TS23 observations yielded a total Na I column density of $\log N = 11.948^{+0.014}_{-0.016}$, and the TS21 observations, $\log N = 11.936^{+0.036}_{-0.060}$. It is encouraging that we arrive at the same total column density, regardless of the resolution, and this provides confidence that we can safely compare the results of observations over the entire range of spectral resolution.

In our sample of multiply observed sight lines, more than 70% show agreement in the total column density to within 3σ. Of those that are discrepant by $>3\sigma$, all but one involve a column density derived from a high-resolution observation that is significantly less than that from a lower-resolution observation. This may result from differing accuracies in the line-spread functions or in the continuum placement. Whatever the cause, the impact of such a systematic error is likely to be less in the highest-resolution data.

In terms of the comparison of individual component fits, while the gross profile is similar, not surprisingly, the narrowest features are lost in the low-resolution spectra. This is clearly seen in our complete sample, in which most of the narrow components are detected in our highest-resolution settings. However, detectability of narrow ISM components is influenced by several other factors other than spectral resolution, including S/N and degree of blending (i.e., proximity in radial velocity to another absorber). Indeed, blending can be so severe, even in the highest-resolution spectra, that the weakest components are unable to be resolved in the fit. Broad features, such as the shallow component near ∼5890.4 Å (at 23.5 km s^{-1}, and with a Doppler parameter of 8.1 km s^{-1}) in the bottom panel of Figure 2 are not necessarily representative of a single ISM structure along that line of sight, but rather a blend of several small absorption features too weak to be resolved into individual components. It is precisely these narrow, weak components – perhaps tracing small but dense ISM clouds – that we hope to identify in the historical solar path, and therefore, while our total column density measurements seem to support the use of a wide range of resolving powers, it is clearly advantageous to use the highest-resolving power possible.

2.4. Comparison With Previous Observations

While this work represents the first densely sampled ISM survey in the direction of the historical solar trajectory, some of our targets had been observed before. Of our sodium observations, 16 of 43 (37%) had been previously observed, and in calcium, 15 of 43 (35%). Most of these were taken as parts of much larger surveys (e.g., Frisch et al. 1990; Welsh et al. 2005), and the relevant references are listed in Tables 4 and 6. While these observations were taken using various instruments and analyzed by different researchers (including some of the earliest high-resolution ISM observations: Adams 1949; Burbidge & Burbidge 1953; Münch & Zirin 1961), they nonetheless provide an interesting comparison.

Overall, in terms of the total column density, there is significant disagreement beyond the 3σ level in the majority of cases for Ca II, while most of the Na I comparisons agree quite well. For Ca II, the most distant targets (i.e., the sight lines with the strongest ISM absorption) tend to agree more closely than the nearest sight lines. A likely explanation is that the systematic errors (e.g., continuum placement, number of assumed components) overwhelm the statistical errors, particularly for sight lines with weak absorption, which is typical for nearby sight lines and Ca II observations. A systematic trend is evident when we compare individual analyses. In Ca II, our measurements are systematically higher (by $\sim$0.4 dex for 4 sight lines) than those same sight lines analyzed by Frisch et al. (1990), while our measurements are systematically lower (by $\sim$0.2 dex for 6 sight lines) than those analyzed by Welsh et al. (2005).

A comparison of individual component fits shows excellent agreement in radial velocity and Doppler parameter for the strongest components. Determining the total number of absorbers appears to be the largest source of disagreement. Strong absorbers may or may not be subdivided depending on the spectral resolution and S/N of the data, and the analysis strategy of the researcher. Given the unavoidable blending along distant sight lines, an accurate inventory of individual absorbers may not be possible, regardless of the quality of the data. Herein lies the inherent limitation of the component fitting technique, and one which we tried to address by using the apparent column density method detailed in Section 3.3.1 and using total column densities in Section 3.3.2. However, if one looks at the profile shapes and integrates individual components into similar radial velocities bins, the agreement can be quite good. Two sight lines (HD34085, Price et al. 2001; HD28497, Blades et al. 1997), both of which were previously observed at high spectral resolution with the UHRF, make for good direct comparisons with our observations. For HD34085 in Ca II, we get an identical fit, differing only in how we interpreted the two most closely spaced blended components in the Price et al. (2001) fit, less than 2 km s^{-1} apart, as a

single absorber in our fit. Similarly for Na I, while the full profile is in good agreement, we typically merge multiple neighboring components (within a few km s^{-1}) identified in Price et al. (2001) into single components, resulting in our fit with 5 components to their fit with 12 components. However, the column-density-weighted radial velocities between our fits match extremely well. The same goes for the comparison with HD28497, where we have slightly lower numbers of components for both Ca II (we have 6 whereas Blades et al. 1997 have 10) and Na I (10 versus 13), but again, the column-density-weighted radial velocities match very well.

A detailed look at previous observations of the same sight lines highlight two important issues that are critical to this work. First, given the impact of systematic errors, it is important to have as close to a homogeneous data sample as possible and to have that data be analyzed uniformly by a single researcher. Second, given unavoidable blending, the results of the traditional technique of fitting a discrete number of components to the absorption profile, need to be augmented by other techniques that can attempt to evaluate the intervening absorption independent of the number of assumed components (see Sections 3.3.1 and 3.3.2).

3. Survey Overview

The final tally of our component fitting analysis yielded 141 individual ISM absorption components in Ca II and Na I toward 43 separate sight lines. The true number of ISM absorbers is probably greater than this based on our inability to resolve the broad shallow components into individual absorbers (23% of all absorbers have $b > 6$ km s^{-1}, mostly in Ca II). Neutral sodium accounted for ∼60% of all detected absorbers (85 components), and calcium the remaining ∼40% (56 components). Calcium components tend to be broader (presumably tracing warmer gas) and the S/N lower than for Na I, which could explain

the lower number of components and higher percentage of broad components. The number of calcium components observed in any sight line with detected absorption ranges from 1–8, with an average of 2.2. For Na I, the number of absorbers ranges from 1–10, with an average of 2.8. In order to compare individual components in both sodium and calcium, we identified paired components, in which the difference in measured interstellar radial velocity is <3 km s^{-1}. Those components that satisfy this requirement (36 in total, 64% of the Ca II sample and 42% of the Na I sample) are identified in the last column of Tables 3 and 5.

Of the 43 sight lines chosen for this study, the nearest 11 sight lines ($d \leq 102.2$ pc) contain no detectable ISM absorption. The observations of these nearest stars are consistent with the low-density interior of the Local Bubble, such that detectable quantities of both ions, particularly Na I, are rare within approximately 100 pc (Lallement et al. 2003). Stronger transitions of more abundant ions are needed to trace the interstellar clouds within the Local Bubble. This is possible only with access to high-resolution spectroscopy in the ultraviolet (UV), where the vast majority of such transitions are found (Redfield 2006).

3.1. Central Velocity

Figure 4 shows the distribution of central velocities of all absorbers for the entire set of sodium and calcium observations. Both the sodium and calcium component velocities range from approximately –40 km s^{-1} to +40 km s^{-1}. The high number of components found around 23 km s^{-1} suggests the presence of a nearby interstellar cloud. Such a large nearby cloud would be seen in absorption toward all stars at increasing distances. Indeed, we associated this absorption with an absorber at or near the Local Bubble boundary, see Section 3.3.1 and 3.3.2). There is a consistent pattern between Na I and Ca II, indicating that to a large degree they are both tracing similar collections of gas.

Figure 5 shows the difference in central velocity for our paired component subsample. While these were defined as paired components based on whether the difference in their velocities was <3 km s^{-1}, the distribution of the velocity differences is typically much less and clearly peaks at zero. However, only 81% of the components are actually consistent with the zero velocity difference at 3σ. While it seems clear that there is often a strong correlation between the sodium and calcium absorption, it is not obvious that they are identically distributed.

3.2. Doppler Parameter

Figure 4 shows the distribution of measured line width, or Doppler parameter, for each component. The high Doppler parameter tail in both the sodium and calcium distributions is a reflection of our inability to resolve the weakest components in the interstellar absorption profile. As a result, multiple weak absorbers that are likely present are blended into broad shallow components. Although the total column density remains the same, it makes it difficult to assess the true number of absorbers and the true line widths. For the entire sample, the median value of the Doppler parameter for Na I is 2.3 km s^{-1} whereas for Ca II it is 4.7 km s^{-1}. However, it is clear from Figure 4 that a distinct population of small Doppler parameter measurements differentiate themselves from the large Doppler parameter tail. For Na I, 61% of the components have $b_{\rm Na} \leq 2.5$ km s^{-1}, with a mean of 1.5 km s^{-1}. For Ca II, 48% of the components have $b_{\rm Ca} \leq 4.8$ km s^{-1}, with a mean of 2.5 km s^{-1}. These values agree fairly well qualitatively with other all-sky surveys. Welty et al. (1994, 1996) find lower median values for Na I (0.73 km s^{-1}) and Ca II (1.31 km s^{-1}), but many of their components have had their Doppler parameters fixed in order to converge on a consistent fit of severely blended lines, which may be biasing their sample to lower values.

3.2.1. Temperature and Turbulent Velocity

Comparison of line widths of ions with different atomic weight that show absorption of the same gas can be used to estimate the temperature and turbulent velocity of that gas. Thermal motions are inversely proportional to the atomic weight while turbulent motions are independent of atomic weight. This relationship is described in the following equation that relates the Doppler width parameter (b [in km s^{-1}]) to the temperature (T [in K]) and nonthermal, turbulent velocity (ξ [in km s^{-1}]),

$$b^2 = \frac{2kT}{m} + \xi^2 = 0.016629\frac{T}{A} + \xi^2, \quad (1)$$

where k is Boltzmann's constant, m is the mass of the ion observed, and A is the atomic weight of the element in atomic mass units. Redfield & Linsky (2004b) did an extensive survey of temperature and turbulent velocity measurements of 50 absorbers within the LISM using line widths of as many as 8 different ions. Their results showed that all observed line widths could be satisfactorily fit with a self-consistent temperature and turbulent velocity. The atomic weight of calcium ($A = 40.08$) is significantly higher than that of sodium ($A = 22.99$), therefore presenting an opportunity in the current survey to disentangle the thermal and turbulent broadening contributions.

As discussed above, the mean values of the Doppler parameter for Ca II are significantly higher than those for Na I. Taken at face value, this is inconsistent with both ions present in a single cloud, characterized by a single temperature and turbulent velocity. This is true for our paired component sample as well. In Figure 6, the Doppler parameter is plotted for both ions. The solid line indicates the relationship of Doppler parameters if purely determined by turbulent motion (i.e., $b_{\rm Na} = b_{\rm Ca}$), whereas the dashed line indicates the scenario in which only thermal motions are included (i.e., $b_{\rm Na} = \sqrt{A_{\rm Ca}/A_{\rm Na}}\, b_{\rm Ca} = 1.320\, b_{\rm Ca}$). In reality, both thermal and turbulent motions likely contribute to the line width, and therefore a collection of gas that includes both ions should fall between these two lines.

For our sample of 36 paired components, only 4 (11%) lie within this self-consistent region, which has been noted in other surveys of Na I and Ca II (e.g., Welty et al. 1996). This argues that these two ions are not well mixed, likely due to differences in the ionization and depletion structure of these two elements. However, based on the correlation in observed radial velocity of the components, it is clear that Na I and Ca II are nonetheless correlated and may simply sample different regions of a typical interstellar cloud structure.

In Figure 4, we convert the observed Doppler line width into the maximum temperature of the gas, assuming that there is no contribution from nonthermal, or turbulent, broadening. If we ignore the high width tails to both distributions and look at the mean values given above in Section 3.2, the mean maximum temperature for Na I is $T_{\rm max} = 3100$ K, and for Ca II, $T_{\rm max} = 15,000$ K. Clearly, Na I is sampling a cooler, and likely less turbulent, interstellar material compared to Ca II. These maximum temperatures are likely significant overestimates of the true temperature, as there is always some contribution to the line broadening via turbulent motions, but serve as a stringent upper limit. The assumption that the sound speed can be used as an upper limit to the turbulent velocity, and therefore provide a lower limit to the temperature of the gas has been applied to evaluations of Ca II line widths (e.g., Welty et al. 1996). This is reasonable for warm partially ionized clouds which typically have subsonic turbulence (e.g., Redfield & Linsky 2004a), but may not be valid for cold neutral clouds probed by Na I absorption which typically have supersonic turbulence (e.g., Heiles & Troland 2003; Meyer et al. 2012).

Instead, here we make some reasonable assumptions about the contribution of the turbulent broadening in order to make a better estimate of the temperature of the gas. The LISM is a convenient standard with which to evaluate Ca II. Not only are the lines widths of many ions detected in the LISM self-consistent along individual sight lines (Redfield & Linsky 2004b), but the entire collection of LISM clouds also are very

similar, and therefore, mean values of line widths of the entire sample are self-consistent, with an average temperature, $T \sim 6900$ K, and turbulent velocity, $\xi \sim 1.67$ km s^{-1} (Redfield & Linsky 2004a). Note that this is subsonic turbulence, typical of warm partially ionized clouds. If we use this same turbulent velocity, for Ca II, this leads to a mean temperature in our sample of ∼8300 K. This turbulent velocity is inconsistent with the average Doppler width of Na I observed in our sample, which again argues that Na I is sampling a distinctly different interstellar environment. If instead, we use the turbulent velocity observed for the Local Leo Cold Cloud ($\xi \sim 0.23$ km s^{-1}; Meyer et al. 2012), which is quite small but supersonic as found for other cold neutral clouds (e.g., Heiles & Troland 2003), it leads to a temperature just slightly less than our maximum temperature, or ∼3000 K. While perhaps correlated, the Na I and Ca II appear to be sampling spatially distinct locations.

3.3. Column Density

Figure 4 shows the distribution of observed individual component column densities determined from our fitting procedure. A distinction here is made between observations with different instruments, which vary in spectral resolution and sensitivity. These both impact our detection limit. The vertical lines indicate those limits for each instrument, which are 3σ upper limits using the mean S/N for observations taken with that instrument. In general, since ISM lines are quite narrow, one gains significantly in sensitivity as one goes to higher spectral resolution. Our calculations support this trend, other than for observations of Na I with TS12, which is significantly less sensitive than the other instruments used at this wavelength, and hence the detection limit is higher than would be expected. The number of weak absorbers is almost certainly underestimated due to the observational bias introduced by our sensitivity limits. As can be seen in the Ca II

distribution, the vast majority of low column density absorbers are detected by our most sensitive (and highest-resolving power) instrument, the UHRF.

The median observed Ca II column density is $\log N(\mathrm{Ca\ II}) \sim 11.3$, and the median observed Na I column density is $\log N(\mathrm{Na\ I}) \sim 11.2$. In Figure 4, the Na I column density has also been translated into a total hydrogen column density. Even though much of the sodium is ionized, Ferlet et al. (1985) demonstrated a correlation exists between Na I and the total hydrogen column density $N(\mathrm{HI} + \mathrm{H_2})$, over Na I column densities consistent with our sample (i.e., $10.0 \leq \log N(\mathrm{Na\ I}) \leq 13.0$). The mean Na I column density thus translates into a mean hydrogen column density of $\log N(\mathrm{HI} + \mathrm{H_2}) \sim 19.5$.

For the purposes of reconstructing the ISM density along the historical solar trajectory, measurements of the column density of each individual absorbing cloud is of the utmost importance. In Paper II, we present an analysis that synthesizes our fits of individual absorbers into an assignment of specific interstellar clouds. However, we can evaluate the column density observed in this direction in even simpler terms which also avoid the bias of component identification. As discussed in Section 2.3, we find that the total column density estimate is unaffected by spectral resolution of the spectrograph, but the identification of individual absorbers is a difficult task, often biased by choices made by the researcher. This is particularly true given the high level of complexity we observe even within a narrow observing cone. We use two techniques that should be relatively free of the choices we made in making the individual fits in order to characterize the variation of column density along the historical solar trajectory. The first is to use the apparent column density, and the other is to simply use the total column density.

3.3.1. Apparent Column Density

In order to characterize the column density structure along this line of sight independent of how individual components are fit to the absorption profile, we employed the apparent column density method described by Savage & Sembach (1991). In this case, the interstellar absorption is analyzed by converting absorption line profiles into profiles of apparent optical depth, $\tau_a(v)$, and apparent column density, $N_a(v)$, per unit velocity. This very quickly provides a diagnostic of the column density and velocity structure regardless of the degree of blending. Apparent optical depth as a function of wavelength is obtained from Equation 2, where $I_0(\lambda)$ is our normalized flux continuum (1 in our case), and $I_{obs}(\lambda)$ is the absorption line profile for a particular observation,

$$\tau_a(\lambda) = ln \left[\frac{I_0(\lambda)}{I_{obs}(\lambda)} \right]. \tag{2}$$

Apparent optical depth is different from true optical depth in that the apparent optical depth has been blurred by the resolution of the instrument used to take the data. In our case, despite using a variety of instruments, they all were sufficiently high resolution that the instrumental impact on the apparent column density measurement is minimal. The apparent optical depth is a good approximation of the true optical depth when the instrument resolution is high, the continuum is well defined, and the measurements have a high signal-to-noise ratio, which is, in general, satisfied by all of our observations. When these conditions are met, $\tau_a(\lambda) \approx \tau(\lambda)$, and we can make use of the relation between true optical depth and column density:

$$\tau(\lambda) = \frac{\pi e^2}{m_e c^2} f \lambda^2 N(\lambda). \tag{3}$$

Total column density can be found from $N = \int N(\lambda) d\lambda$ and expressing total column

density as a function of velocity, we can solve Equation 3 for $N(v)$ and integrate, giving:

$$N = \frac{m_e c}{\pi e^2 f \lambda} \int ln \frac{I_0(v)}{I(v)} dv, \tag{4}$$

where m_e is the mass of an electron, f is the transition oscillator strength, c is the speed of light, and λ is wavelength in Ångstroms. Apparent column density per unit velocity as a function of distance is plotted in Figure 7 for the sodium and calcium data. As was discussed above, the sodium column density has been translated into hydrogen column densities following the relationship derived by Ferlet et al. (1985).

The onset of detected absorption is at a similar distance for both ions and consistent with the edge of the Local Bubble at ∼120 pc. Shortly thereafter, there is a strong absorption feature at ∼23 km s^{-1} that is consistently seen in absorption profiles at increasing distances. This suggests that there is a cloud at or near the edge of the Local Bubble taking up a significant portion of the sample area. Given the peculiar motion of the Sun (13.38 km s^{-1}), it will travel this equivalent distance in ∼10 Myr. Unfortunately, Ca II and Na I are largely insensitive to the warm, partially ionized clouds that are known to reside within the Local Bubble, which require UV spectroscopic observations (Frisch et al. 2011).

The sodium and calcium apparent column density plots look very similar, again arguing for a correlation in the spatial distribution of Na I and Ca II. The broader profiles of Ca II are also evident in Figure 7.

3.3.2. Total Column Density

An additional technique to evaluate the column density along this unique direction is to work with the total observed column density. Again, this is independent of the strategy of component fitting and appears robust to a wide range of resolving powers. The total

column densities for sight lines in our sample are listed in Tables 4 and 6. Figure 8 displays these values as a function of distance. Again, insensitive to the low column densities of the LISM clouds within the Local Bubble, our nearest sight lines provide only upper limits. The edge of the Local Bubble is clearly seen at ∼120 pc, with a rapid increase in total column density, which quickly levels off. Our measurements of the distance to the edge of the Local Bubble are in agreement with Lallement et al. (2003) who did an all-sky survey of interstellar neutral sodium out to a distance of 500 parsecs. This sharp rise is most apparent in the sodium column density profile but is also seen in the calcium data. The error in the distance measurements is from *Hipparcos* parallax measurements (van Leeuwen 2007), and for this reason, the error bars tend to grow with distance as parallax becomes more difficult to measure.

The spread in column densities at any given distance is likely an indication that we are observing small-scale structure variations in the ISM across this relatively narrow observing cone. At the largest distances (∼500 pc), targets at the edge of our observing cone would be separated from the center by a physical distance of 80 pc. These spatial variations could explain drops in the total column density for sight lines at larger distances in Figure 8 as well as the apparent disappearance and reappearance of absorbing components in the apparent column density profiles presented in Figure 7.

In order to evaluate the spatial variations in our sample, the total column density measurements were analyzed to see if a self-consistent series of absorbers within individual distance bins could replicate our observations. We used distance bins of <150 pc, 150–200 pc, 200–250 pc, 250–350 pc, and 350–700 pc. A minimum curvature surface interpolation is made using the measurements toward targets that fall within these distance bins. More distant targets provide limits to the column density of preceding distance bins. Once a spatial map of column density is determined for the closest distance bin, it is subtracted

from more distant sight lines and the procedure is repeated for the next distance bin. Despite this being the most densely sampled high-resolution absorption line survey of an individual sight line, we are still left with only 43 pencil-beam measurements. Given the large distances of some of our sight lines, the physical spacings can be quite dramatic. For example, in the farthest distance bin, with a mean distance of 525 pc, the radius of our field of view (10°) is equivalent to 92.6 pc, whereas for our closest bin with a mean distance of 125 pc such an angular separation is only 22.0 pc. Nonetheless, a self-consistent model of the spatial variation of column density in both Ca II and Na I can be made. The results are shown in Figure 9. Overall, both ions show a similar, although not identical, spatial distribution. Again, this argues for correlated, though not necessarily identical, distributions of Ca II and Na I. Additionally, significant structure is observed, highlighting the complexity of the ISM and need for densely sampled surveys in order to characterize this complexity.

3.3.3. Na I/Ca II Ratio

Neutral sodium and singly ionized calcium are two of the strongest resonance lines in the optical (Redfield 2006) and have therefore been extensively used to diagnose the physical properties of the ISM over a range of conditions. Measuring the column density ratio of these two ions, which is relatively simple observationally, holds the promise of evaluating the impact of ionization and depletion, both of which will impact the ratio. In the diffuse, warm ISM, both Na I and Ca II are trace species, with Na II and Ca III dominating (Slavin & Frisch 2002). Additionally, the two elements have very different condensation temperatures and therefore, have very different patterns of depletion onto dust, namely calcium is typically depleted in the gas phase by more than two orders of magnitude compared to sodium (Savage & Sembach 1996). For these reasons, the Na I/Ca II column

density ratio can vary by several orders of magnitude and potentially be a sensitive diagnostic of these phenomena. In our sample of paired components, we see column density ratios that range more than two orders of magnitude from N(Na I)/N(Ca II) =0.066–12 (see Figure 10), while even larger variations have been detected along other sight lines (Welty et al. 1996).

Based on many studies of Na I and Ca II (e.g., Routly & Spitzer 1952; Siluk & Silk 1974; Crawford 1992; Bertin et al. 1993; Welty et al. 1996), the largest column density ratio ranges tend to be associated with cold ($T \sim 100$ K), dense interstellar clouds, where Na I is prevalent, Ca II is rare, and calcium in general is significantly depleted onto dust. The lowest column density ratios are typically associated with warm ($T \sim 1000$ K), high-velocity interstellar environments (e.g., supernova remnants and shells; Siluk & Silk 1974), where dust has either been destroyed and the constituents returned to the gas phase, or where depletion has not yet initiated. We certainly see evidence to support this in our sample, in which the largest Na I/Ca II values are located just beyond the Local Bubble boundary (see Figures 10 and 11), which delineates the warm, rarefied Local Bubble gas from dense molecular gas. Our dense survey of nearby stars, which have accurate distance measurements, allows us to pinpoint the location of the high column density ratio gas.

Additional evidence of the physical conditions of gas with different Na I/Ca II ratios comes in the form of the Routly-Spitzer Effect (Routly & Spitzer 1952), which is exemplified in a canonical figure of observed ISM velocity versus column density ratio. We show this figure for our own sample at the top of Figure 10. The highest Na I/Ca II column density ratios tend to be at low velocity, whereas the highest velocities tend have low column density ratios. Siluk & Silk (1974) presented the interpretation that these high peculiar velocities could be signatures of old supernova remnants and that shocks associated with these remnants would preferentially destroy dust grains and enhance the gas phase calcium

abundance, thereby lowering the Na I/Ca II column density ratio. Our sample also shows the canonical Routly-Spitzer Effect, and the majority of the low column density ratio measurements are associated with our longest sight lines, which likely traverse a wide range of interstellar environments.

Finally, in Figure 10, we also see a tight correlation between the Na I/Ca II column density ratio and Na I column density, which as mentioned above is correlated with hydrogen column density (Ferlet et al. 1985). While observational bias could influence this plot, as shown in Figure 4, our detection limits are low enough as to not significantly impact the observed correlation. Instead, it is likely that the variation in calcium depletion is the cause of the correlation. The largest sodium column densities are likely indicative of the densest interstellar environments, in which calcium can be depleted by more than 3 orders of magnitude, whereas sodium maintains a modest depletion over a wide range of densities (Phillips et al. 1984).

While these connections between the Na I/Ca II column density ratio and other physical quantities imply a physical association, we know from the comparison of the Doppler parameter shown in Figure 6, that Na I and Ca II are not identically distributed. Because they do not share an identical temperature or turbulent velocity, they cannot be components of the same parcel of gas. Routly & Spitzer (1952) made note of the inconsistent differences in the Doppler parameter between sodium and calcium but, given the moderate spectral resolution of the observations, the larger Ca II line widths could be the result of component blending, which due to the Routly-Spitzer Effect will be more significant for Ca II than Na I. In essence, the low Na I/Ca II column density ratio, for which, by necessity, there would be a strong Ca II signal, is also found at a wide range of velocities, and so the blending of these lines would lead to a large Doppler width. However, as the spectral resolution of observations has improved, the low column density ratio sight

lines have not resolved into a series of blended interstellar components. More than half of our paired sample were taken from the highest-resolution spectrographs used in this survey, and yet the line width discrepancy, $b_{\rm Ca} > b_{\rm Na}$ still holds. This makes using the ionization and depletion to derive fundamental physical properties (e.g., electron density, temperature) problematic. Slavin & Frisch (2008), using a series of photoionization models of the local interstellar medium, also emphasize the difficulty in using this ratio of trace species as a diagnostic of physical properties in warm partially ionized clouds. In addition, a third possibility needs to be explored to explain the observed Na I/Ca II column density ratio, and that is geometry. Because we do not know how Na I and Ca II are distributed in space, the orientation of the absorbing clouds, particularly if they are filamentary, can have a significant impact on the Na I/Ca II column density ratio. Filamentary structures are quite common in the ISM (Frisch & York 1983; Heiles 1997; Redfield & Linsky 2008; Peek et al. 2011), presumably organized by the presence of magnetic fields (Jackson et al. 2003). So, for example, at the Local Bubble boundary, where there is likely to be interactions between the hot Local Bubble gas and the cold, dense molecular material, the orientation of structures at this interface may play a significant role in the large range of Na I/Ca II column density ratios.

3.4. Small-Scale Structure

In this section, we examine the subset of sight lines that are close in angle in order to search for evidence of small-scale structure in the ISM along our observing cone. There are 5 sight line pairs that are within 1° of each other and show ISM absorption: HD30963–HD31089, 0.31°; HD30535–HD30679, 0.57°; HD27563–HD27436, 0.60°; HD28763–HD28497, 0.82°; HD28843–HD29248, 0.93°. Of particular note are the first two pairs listed (HD30963–HD31089 and HD30535–HD30679) because they are within

2° of the solar trajectory direction. A detailed comparison between the sight lines is not discussed here, as interested readers can easily make their own comparisons using the spectra in Figures 3a–3o, and Tables 3 and 5, but we do highlight a common occurrence in many of the pairs that argues for the existence of small-scale structure. Excess absorption is often detected in the closer of the two targets, requiring that the absorption discrepancy between the sight lines occur interior to the nearest star. For example, HD30963 shows significant Na I absorption at velocities <10 km s^{-1}, whereas HD31089 shows none, which is in contrast to the Na I absorption near 20 km s^{-1}, which increases by about a factor of 3 between HD30963 and HD31089. Likewise, HD30535, which is significantly closer than HD30679, shows Na I absorption near 20 km s^{-1} that is about twice that of the absorption at the same velocity in the more distant target HD30679. Finally, the last listed pair (HD28843–HD29248) is also of interest because it is the closest of the pairs, with stellar distances of 145.8 pc and 207.0 pc, respectively, and hence the distance errors are small (<10 pc). This pair also shows excess absorption (near 0 km s^{-1}) in the spectrum of the closer star for both Na I and Ca II. For the three cases discussed above, the maximum size scale of the variation (i.e., the projected length between the two stars at a distance just interior to the nearest star), is 1.3, 3.3, and 2.4 pc, respectively, although if the variation is assumed to be at the Local Bubble boundary at 120 pc, the scale of ISM variation is even smaller at only 0.6, 1.2, and 1.9 pc, respectively.

Others sight line pairs of interest include those with small physical separations. These tend to be pairings of the closest targets at essentially identical distances. There are 13 pairs in which the physical separation is ≤15 pc. More than half of these include pairings between the targets within the Local Bubble and therefore, have no detected absorption. However, there are 5 pairings in which both have detected absorption, including HD28208 and HD28980 with a physical separation of 7.7 pc, and HD31512 and HD32249 with a separation of 9.4 pc. Again, despite being at practically identical distances, there are

significant differences in the ISM absorption profile. The Na I column densities differ by a factor of 3 between HD28208 and HD28980, and by a factor of 2 between HD31512 and HD32249. The Ca II is similar between the pairs, but still shows variations in observed velocity (e.g., HD28208–HD28980) and component structure (e.g., HD31512–HD32249).

Variations in the ISM on a small scale (i.e., sub-parsec) have been found in many other observations, including wide binaries (Meyer & Blades 1996; Watson & Meyer 1996), and high proper motion pulsars (Frail et al. 1994; Stanimirović et al. 2010). Only in the very closest ISM, primarily observed in the UV using dominant ionization stage ions, do we see little evidence for small-scale structure, but instead coherent absorption over large angles (Redfield & Linsky 2001). While a large coherent pattern of absorption is evident in our sample (see Figure 7) a detailed look at practically any pair of sight lines, shows significant discrepancies, indicating a fundamental complexity in the distribution and/or physical properties of the observed ISM. In the context of reconstructing the ISM along the historical solar trajectory, this small-scale structure makes it very difficult to identify anything other than the largest structures. However, it motivates even more strongly the need to understand the interaction between stars and the ISM through which they are passing because the abundance of small-scale structures implies that dramatic changes in the properties of our surrounding ISM are a common occurrence.

4. Conclusions

We performed the densest ISM survey at high spectral resolution, observing 43 targets within 9 degrees of the historical solar trajectory out to a distance of ∼500 pc. Observations were taken of Na I and Ca II at resolving powers ranging from $60,000 < R < 940,000$. We fit the absorption profiles with 85 Na I and 56 Ca II components.

1. Component analysis is consistent between observations over a range of resolving powers, although the highest spectral resolution provides the highest sensitivity to narrow and low column density absorbers. The total column density appears insensitive to resolution among observations in our study and even to analysis strategy among similar observations analyzed by other researchers.

2. However, the number of components, which has a significant impact on measured line widths, velocities, and individual column densities, is variable depending on resolving power, S/N, and researcher. This argues for a homogeneous data set analyzed together, as has been done for this sample. In addition, we present two alternative techniques to assess the ISM profile along the direction of the historical solar trajectory: the apparent column density and the total column density.

3. The nearest significant ISM absorber has a velocity of $\sim$23 km s^{-1} and is located at $\sim$120 pc, which is consistent with the edge of the Local Bubble. This interstellar material would have been encountered by the Sun $\sim$10 Myr ago. However, we know that significant interstellar material resides within this volume, including the LIC, which defines the current structure of the heliosphere. These optical transitions are simply not sensitive enough to probe the very closest material, and therefore, to measure the ISM that the Sun encountered within the last few million years, we need spectroscopic observations in the UV.

4. Na I and Ca II do not seem to be identically distributed in interstellar clouds, as indicated by the inconsistency of the line widths, namely that $b_{\rm Ca} > b_{\rm Na}$, despite the fact that calcium has a higher atomic weight. Nonetheless, the two ions do appear to be correlated, given the similarity in velocity structure and therefore, are likely constituents in related but distinct structures within a single ISM cloud complex, with Ca II tracing warm ($\sim$8000 K) gas and Na I tracing cold ($<$3000 K) gas.

5. The Na I/Ca II column density ratio shows the largest variation at the Local Bubble boundary, possibly due to the complexity of physical conditions near that interface (e.g., temperature, ionization, depletion) or variations in orientation of the dissimilar distributions of Na I and Ca II. Given that these two ions are not identically distributed, it makes using the column density ratio problematic in evaluating ionization and depletion effects. Indeed, the non-coincident spatial distribution of the Na I and Ca II in these clouds, and their possibly independent orientation along the line of sight, may also have a large role in determining the column density ratio that is observed.

6. Significant spatial variation is detected, although individual absorbers are consistently detected in practically all sight lines (e.g., the 23 km s^{-1} component). A corollary to this conclusion is that small-scale structure is observed to be ubiquitous, again arguing for complexity in cloud structure or distribution. While this makes a reconstruction of the ISM more difficult, it makes it clear that dramatic variations in interstellar density are a common occurrence and that understanding the interaction between the ISM and the Sun, together with the heliosphere and the planets, is important.

The connection between the ISM and ultimately planets, via a dynamic heliosphere is captivating, but also complex. The work presented here lays the foundation for evaluating this relationship by presenting observations and analysis of the interstellar medium along the historical solar trajectory, the material that the Sun is likely to have interacted within the last ∼40 million years. There are many additional questions and assumptions that must be addressed before one is able to use these observations to make predictions regarding the influence on planets. For example, an estimate of the volume density is critical, but difficult to obtain. We will explore several options in Paper II, including calculating the density using the column density and distance differences between the sight line where the absorption

is first detected and the sight line just preceding in distance in which the absorption is not detected. Alternatively, we can make order of magnitude estimates from assuming the spatial extent is comparable to the radial extent, or simply using canonical cloud sizes derived from other work. Volume densities will then allow us to calculate heliospheric compression and the implications for phenomena that may affect planets (e.g., the cosmic ray flux). These topics are discussed more in depth in Paper II. While this work is clearly tied to the Sun and heliosphere, these same issues are at work for other planet-bearing stars and their own surrounding interstellar environments. Indeed, the vast majority of known exoplanets reside within $\sim$500 pc, and therefore are encountering interstellar clouds not all that different from those studied here. If an ISM-planet connection can be established, it may have important consequences for evaluating the long-term evolution of the atmospheres of these planets.

We are grateful to the staff at the McDonald Observatory, in particular David Doss, and at the Anglo-Australian Observatory, in particular Stuart Ryder. Their assistance was essential to the success of the observations that were acquired for this work. K.W. would like to thank S.R. for his support and guidance throughout this master's thesis project.

Facilities: Smith (TS12,TS21,TS23) AAT (UHRF)

REFERENCES

Adams, W. S. 1949, ApJ, 109, 354

Albert, C. E., Blades, J. C., Morton, D. C., Lockman, F. J., Proulx, M., & Ferrarese, L. 1993, ApJS, 88, 81

Begelman, M. C., & Rees, M. J. 1976, Nature, 261, 298

Beintema, D. 1975, PhD thesis, , Univ. Groningen, (1975)

Bertin, P., Lallement, R., Ferlet, R., & Vidal-Madjar, A. 1993, A&A, 278, 549

Bevington, P. R. 2003, Data Reduction and Error Analysis for the Physical Sciences (McGraw-Hill)

Blades, J. C., Sahu, M. S., He, L., Crawford, I. A., Barlow, M. J., & Diego, F. 1997, ApJ, 478, 648

Burbidge, E. M., & Burbidge, G. R. 1953, ApJ, 117, 465

Crawford, I. A. 1992, MNRAS, 259, 47

Decker, R. B., Krimigis, S. M., Roelof, E. C., Hill, M. E., Armstrong, T. P., Gloeckler, G., Hamilton, D. C., & Lanzerotti, L. J. 2005, Science, 309, 2020

Dehnen, W., & Binney, J. J. 1998, MNRAS, 298, 387

Diego, F., et al. 1995, MNRAS, 272, 323

Fahr, H. J. 1968, Ap&SS, 2, 474

Ferlet, R., Vidal-Madjar, A., & Gry, C. 1985, ApJ, 298, 838

Frail, D. A., Weisberg, J. M., Cordes, J. M., & Mathers, C. 1994, ApJ, 436, 144

Frisch, P., & York, D. G. 1986, in The Galaxy and the Solar System, ed. R. Smoluchowski, J. M. Bahcall, & M. S. Matthews, 83–100

Frisch, P. C. 2006, in Astrophysics and Space Science Library, Vol. 338, Solar Journey: The Significance of our Galactic Environment for the Heliosphere and Earth, ed. P. C. Frisch (Dordrecht: Springer)

Frisch, P. C., Redfield, S., & Slavin, J. D. 2011, ARA&A, 49, 237

Frisch, P. C., Sembach, K., & York, D. G. 1990, ApJ, 364, 540

Frisch, P. C., & York, D. G. 1983, ApJ, 271, L59

Génova, R., & Beckman, J. E. 2003, ApJS, 145, 355

Giacalone, J., & Jokipii, J. R. 1999, ApJ, 520, 204

Grenier, S., Baylac, M., Rolland, L., Burnage, R., Arenou, F., Briot, D., Delmas, F., Duflot, M., Genty, V., Gómez, A. E., Halbwachs, J., Marouard, M., Oblak, E., & Sellier, A. 1999, A&AS, 137, 451

Habing, H. J. 1969, Bull. Astron. Inst. Netherlands, 20, 177

Hearty, T., Fernández, M., Alcalá, J. M., Covino, E., & Neuhäuser, R. 2000, A&A, 357, 681

Heiles, C. 1997, ApJ, 481, 193

Heiles, C., & Troland, T. H. 2003, ApJ, 586, 1067

Hobbs, L. M. 1969, ApJ, 157, 165

—. 1974, ApJ, 191, 381

—. 1978, ApJS, 38, 129

—. 1984, ApJS, 56, 315

Holweger, H., Hempel, M., & Kamp, I. 1999, A&A, 350, 603

Hoyle, F., & Lyttleton, R. A. 1939, in Proceedings of the Cambridge Philosophical Society, Vol. 35, Proceedings of the Cambridge Philosophical Society, 405

Jackson, T., Werner, M., & Gautier, III, T. N. 2003, ApJS, 149, 365

Lallement, R., Bertin, P., Chassefiere, E., & Scott, N. 1993, A&A, 271, 734

Lallement, R., Welsh, B. Y., Vergely, J. L., Crifo, F., & Sfeir, D. 2003, A&A, 411, 447

Linsky, J. L., & Wood, B. E. 1996, ApJ, 463, 254

Magnani, L., Blitz, L., & Mundy, L. 1985, ApJ, 295, 402

Makaganiuk, V., Kochukhov, O., Piskunov, N., Jeffers, S. V., Johns-Krull, C. M., Keller, C. U., Rodenhuis, M., Snik, F., Stempels, H. C., & Valenti, J. A. 2011, A&A, 529, A160

Meyer, D. M., & Blades, J. C. 1996, ApJ, 464, L179

Meyer, D. M., Lauroesch, J. T., Heiles, C., Peek, J. E. G., & Engelhorn, K. 2006, ApJ, 650, L67

Meyer, D. M., Lauroesch, J. T., Peek, J. E. G., & Heiles, C. 2012, ApJ, 752, 119

Morton, D. C. 2003, ApJS, 149, 205

Müller, H.-R., Frisch, P. C., Florinski, V., & Zank, G. P. 2006, ApJ, 647, 1491

Münch, G., & Zirin, H. 1961, ApJ, 133, 11

Nordström, B., Mayor, M., Andersen, J., Holmberg, J., Pont, F., Jørgensen, B. R., Olsen, E. H., Udry, S., & Mowlavi, N. 2004, A&A, 418, 989

O'dell, C. R. 2001, ARA&A, 39, 99

Pavlov, A. A., Toon, O. B., Pavlov, A. K., Bally, J., & Pollard, D. 2005, Geophys. Res. Lett., 32, L03705

Peek, J. E. G., Heiles, C., Peek, K. M. G., Meyer, D. M., & Lauroesch, J. T. 2011, ApJ, 735, 129

Penprase, B. E. 1993, ApJS, 88, 433

Phillips, A. P., Pettini, M., & Gondhalekar, P. M. 1984, MNRAS, 206, 337

Press, W. H., Teukolsky, S. A., Vetterling, W. T., & Flannery, B. P. 2002, Numerical recipes in C++ : the art of scientific computing

Price, R. J., Crawford, I. A., Barlow, M. J., & Howarth, I. D. 2001, MNRAS, 328, 555

Redfield, S. 2006, in Astronomical Society of the Pacific Conference Series, Vol. 352, New Horizons in Astronomy: Frank N. Bash Symposium, ed. S. J. Kannappan, S. Redfield, J. E. Kessler-Silacci, M. Landriau, & N. Drory, 79

Redfield, S., & Linsky, J. L. 2000, ApJ, 534, 825

—. 2001, ApJ, 551, 413

—. 2002, ApJS, 139, 439

—. 2004a, ApJ, 602, 776

—. 2004b, ApJ, 613, 1004

—. 2008, ApJ, 673, 283

Routly, P. M., & Spitzer, Jr., L. 1952, ApJ, 115, 227

Savage, B. D., & Sembach, K. R. 1991, ApJ, 379, 245

—. 1996, ARA&A, 34, 279

Scherer, K., Fichtner, H., Borrmann, T., Beer, J., Desorgher, L., Flükiger, E., Fahr, H.-J., Ferreira, S. E. S., Langner, U. W., Potgieter, M. S., Heber, B., Masarik, J., Shaviv, N., & Veizer, J. 2006, Space Sci. Rev., 127, 327

Schönrich, R., Binney, J., & Dehnen, W. 2010, MNRAS, 403, 1829

Shapley, H. 1921, Journal of Geology, 29, 502

Shaviv, N. J. 2003, New A, 8, 39

Shorlin, S. L. S., Wade, G. A., Donati, J., Landstreet, J. D., Petit, P., Sigut, T. A. A., & Strasser, S. 2002, A&A, 392, 637

Shull, J. M., York, D. G., & Hobbs, L. M. 1977, ApJ, 211, L139

Siluk, R. S., & Silk, J. 1974, ApJ, 192, 51

Slavin, J. D., & Frisch, P. C. 2002, ApJ, 565, 364

—. 2008, A&A, 491, 53

Smith, D. S., & Scalo, J. M. 2009, Astrobiology, 9, 673

Stanimirović, S., Weisberg, J. M., Pei, Z., Tuttle, K., & Green, J. T. 2010, ApJ, 720, 415

Stawikowski, A., & Glebocki, R. 1994, Acta Astron., 44, 33

Talbot, R. J., Butler, D. M., & Newman, M. J. 1976, Nature, 262, 561

Thaddeus, P. 1986, The Galaxy and the Solar System, 61

Tody, D. 1993, in Astronomical Society of the Pacific Conference Series, Vol. 52, Astronomical Data Analysis Software and Systems II, ed. R. J. Hanisch, R. J. V. Brissenden, & J. Barnes, 173–+

Tull, R. G. 1972, in Proc. ESO/CERN Conference on Auxiliary Instrumentation for Large Telescopes (Geneva: ESO), 259

Tull, R. G., MacQueen, P. J., Sneden, C., & Lambert, D. L. 1995, PASP, 107, 251

Usoskin, I. G., Alanko-Huotari, K., Kovaltsov, G. A., & Mursula, K. 2005, Journal of Geophysical Research (Space Physics), 110, 12108

Vallerga, J. V., Vedder, P. W., Craig, N., & Welsh, B. Y. 1993, ApJ, 411, 729

van Leeuwen, F. 2007, A&A, 474, 653

Watson, J. K., & Meyer, D. M. 1996, ApJ, 473, L127

Welsh, B. Y., Craig, N., Vedder, P. W., & Vallerga, J. V. 1994, ApJ, 437, 638

Welsh, B. Y., Sallmen, S., & Jelinsky, S. 2005, A&A, 440, 547

Welsh, B. Y., & Shelton, R. L. 2009, Ap&SS, 323, 1

Welsh, B. Y., Vedder, P. W., Vallerga, J. V., & Craig, N. 1991, ApJ, 381, 462

Welty, D. E., Hobbs, L. M., & Kulkarni, V. P. 1994, ApJ, 436, 152

Welty, D. E., Morton, D. C., & Hobbs, L. M. 1996, ApJS, 106, 533

Wood, B. E., Müller, H.-R., Zank, G., Linsky, J., & Redfield, S. 2005, ApJ, 628, L143

Wyman, K., & Redfield, S. 2013, in preparation

Zank, G. P., & Frisch, P. C. 1999, ApJ, 518, 965

This manuscript was prepared with the AAS LaTeX macros v5.2.

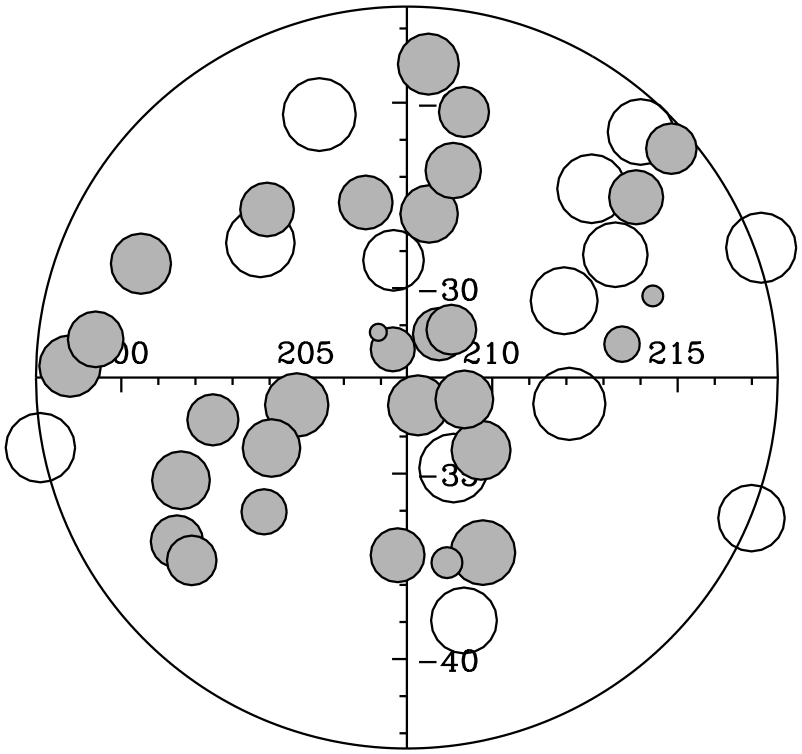

Fig. 1.— Distribution of sight lines used in this survey and listed in Table 1. We observed 43 stars within 9° of the historical solar trajectory at the origin ($l_0 = 207.70°$ and $b_0 = -32.41°$; Dehnen & Binney 1998). More than 50% of the sample is within ∼5° of the solar trajectory. In addition, 8 sight line pairs are separated from each other by <1°. Symbol size is inversely proportional to stellar distance, which extends from 27.40–610 pc. Open symbols indicate no ISM absorption was detected (almost exclusively targets within 120 pc), while shaded symbols indicate absorption profiles that were fit in order to reconstruct the interstellar environments along the historical solar trajectory.

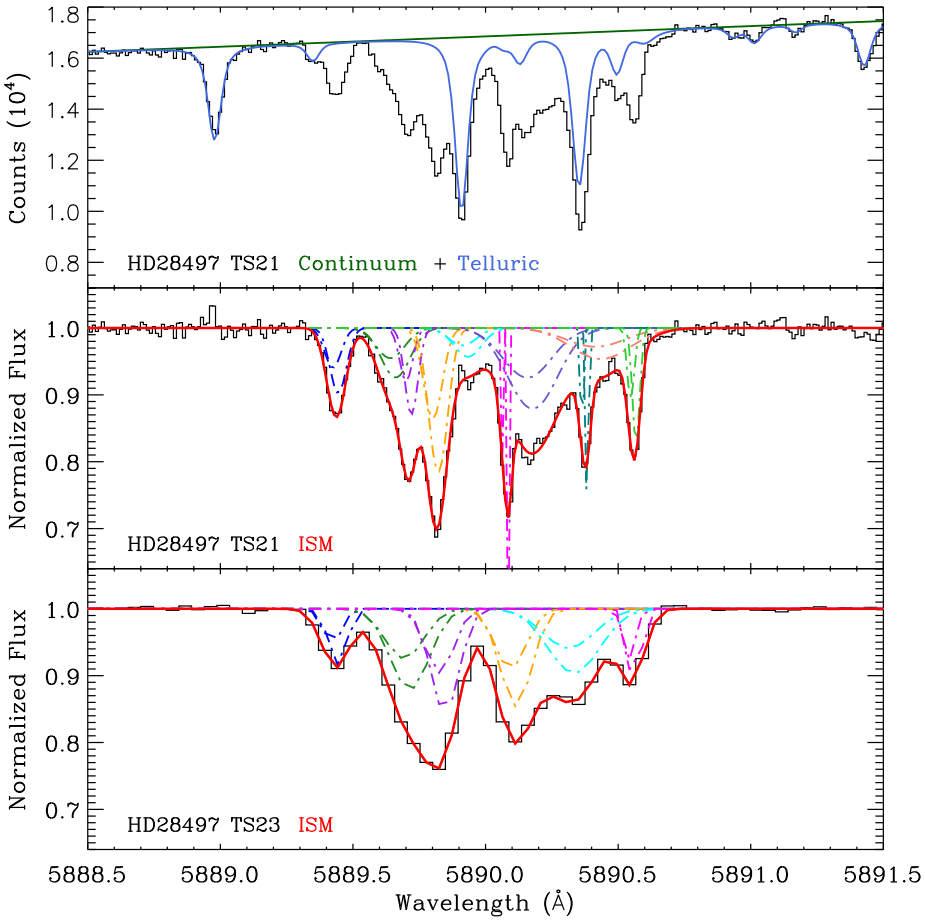

Fig. 2.— HD28497 Na I continuum normalization, telluric line fitting, and ISM absorption observed at two spectral resolutions. The top panel is data showing the continuum modeled with a low-order polynomial along with a fit to the telluric contamination. The bottom two panels are the data after normalization and subtraction of the telluric features, where the middle panel is data taken with TS21 at a resolution of $R \sim 240{,}000$, and the bottom panel was taken with TS23 at a resolution of $R \sim 60{,}000$. Strong absorbers, particularly if unblended (e.g., the most blueshifted component), are consistent between the two observations, but the narrowest absorbers (i.e., $b < 1$ km s^{-1}) seen in the higher-resolution observation fail to be resolved in the lower-resolution observation. However, both these observations yield the same measurement of total column density (within the errors) along this particular sight line (TS23: N(Na I) $= 11.948^{+0.014}_{-0.016}$, TS21: N(Na I) $= 11.936^{+0.036}_{-0.060}$). Results of other sight lines observed at different spectral resolution are compared in Table 7

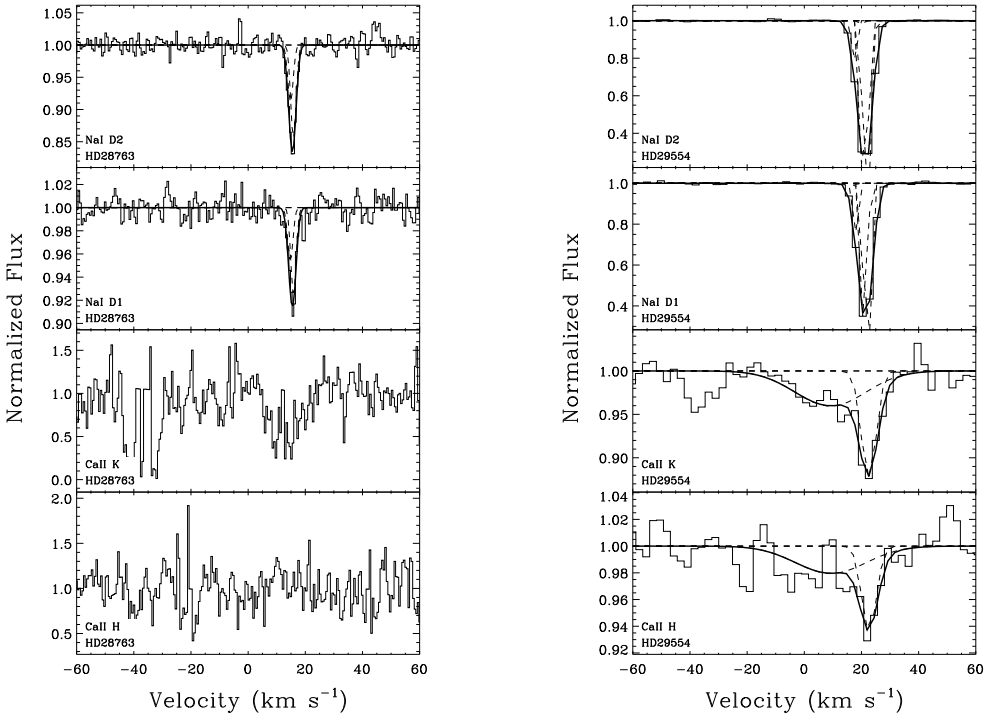

Fig. 3a.— Fits to high-resolution Na I and Ca II spectra that show ISM absorption toward stars along the historical solar trajectory. The spectra have been normalized (thin solid line). If absorption is detected, dashed lines indicate the profile of individual absorbers (dashed lines), while the thick solid line is the total absorption of all components convolved with the instrumental line-spread function. Fit parameters based on these fits are listed in Tables 3 and 5.

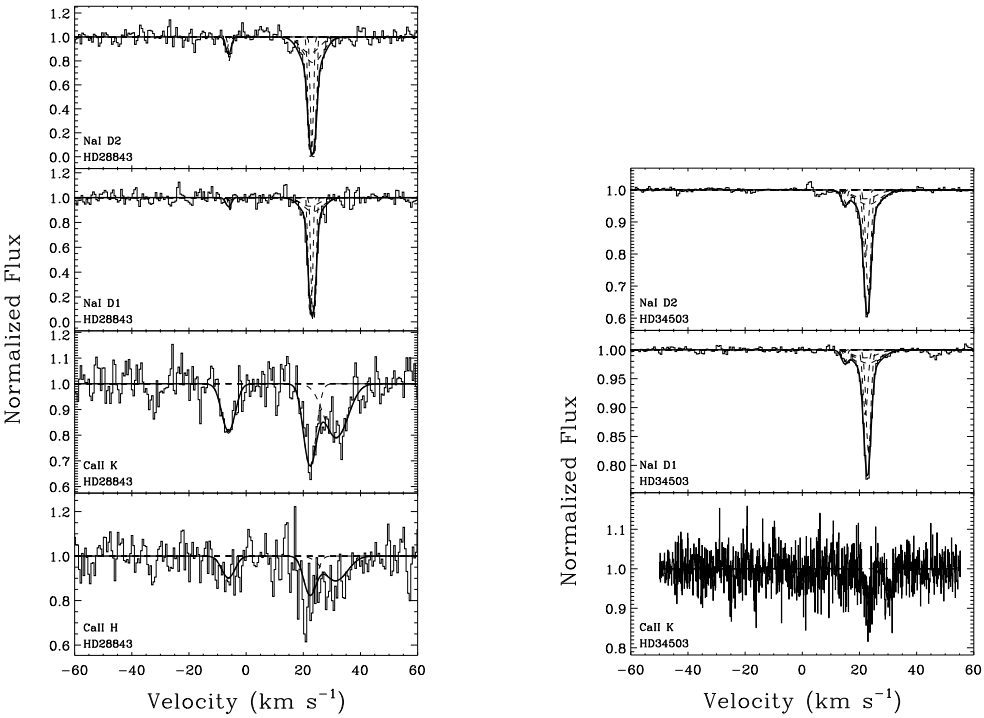

Fig. 3b.— Same as Figure 3a

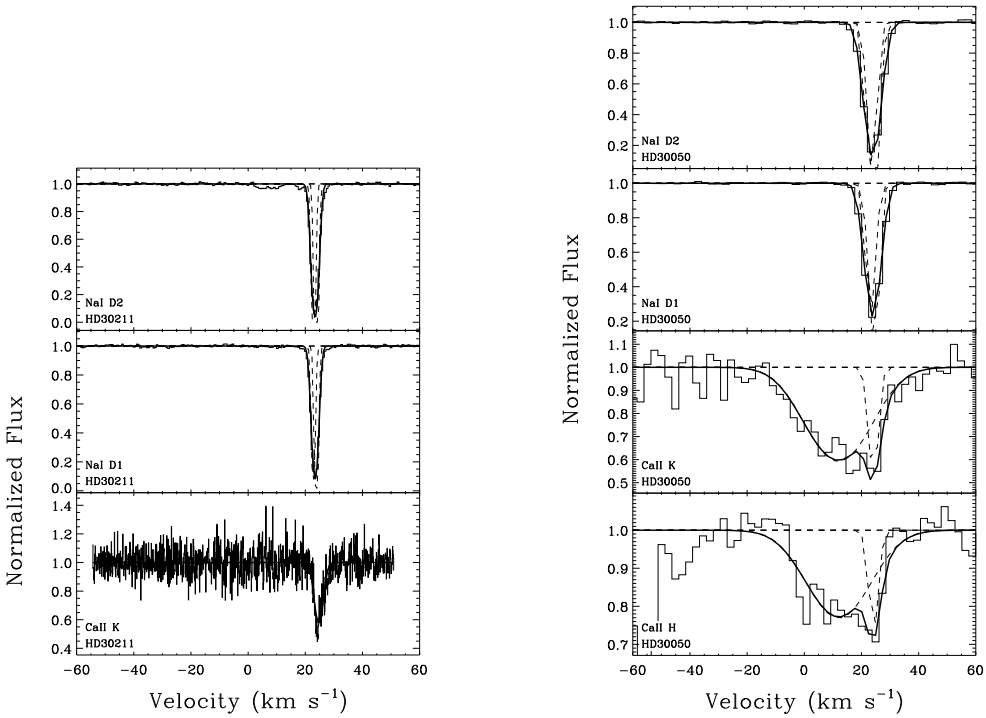

Fig. 3c.— Same as Figure 3a

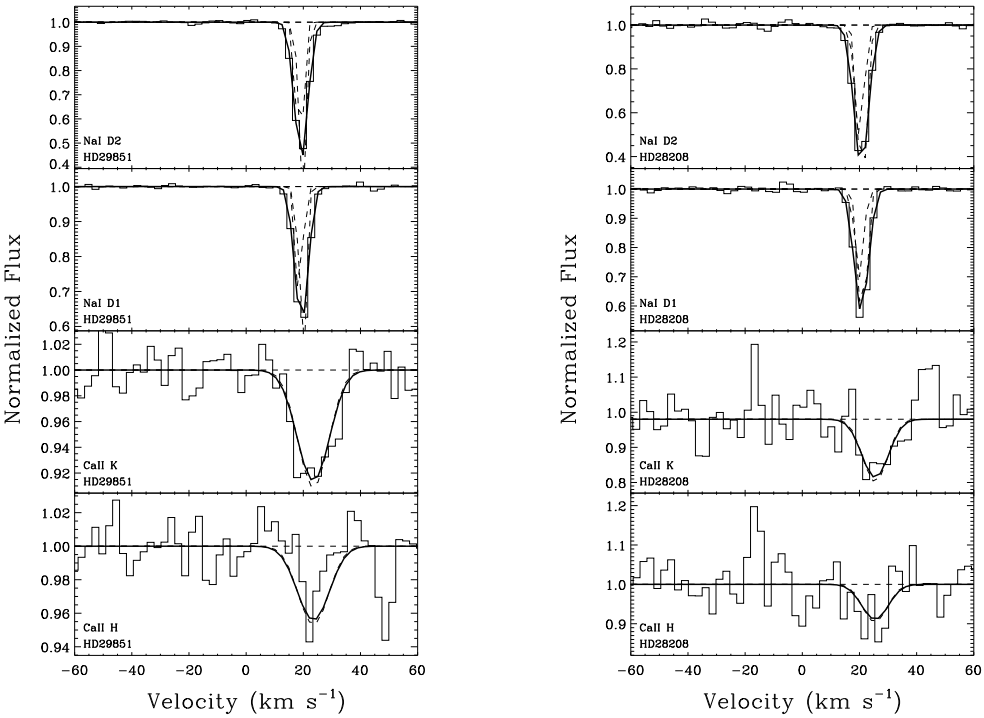

Fig. 3d.— Same as Figure 3a

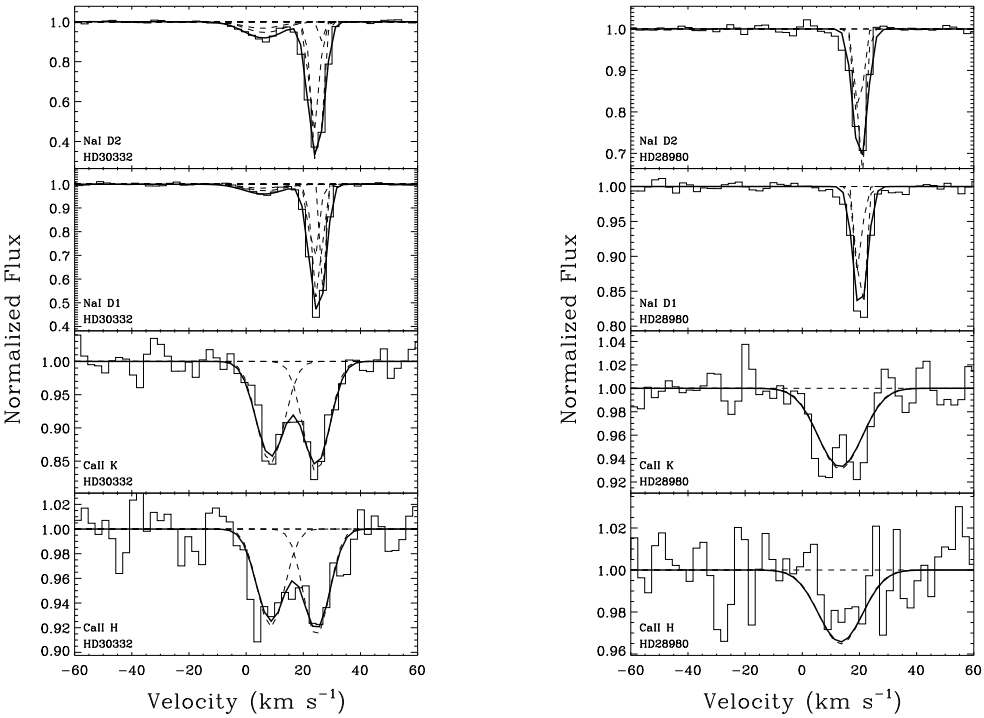

Fig. 3e.— Same as Figure 3a

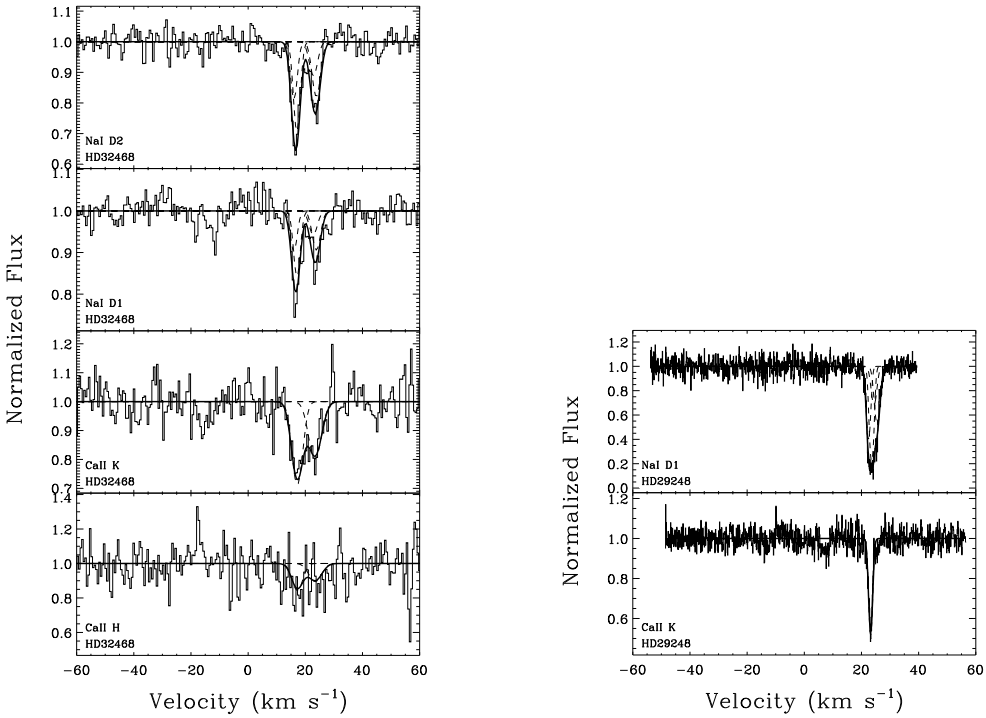

Fig. 3f.— Same as Figure 3a

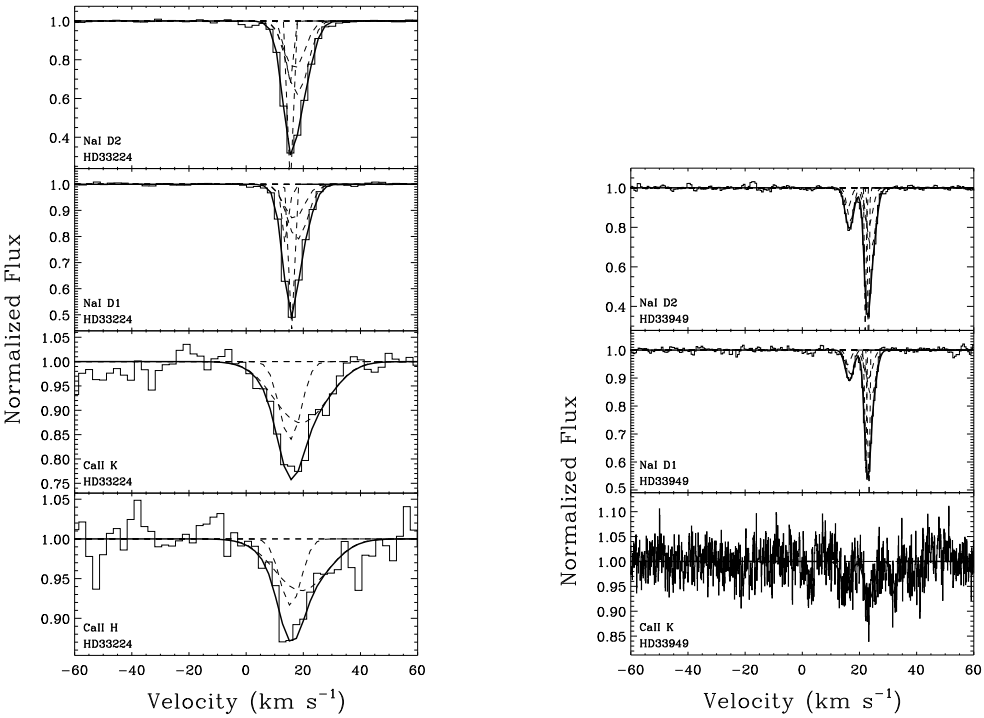

Fig. 3g.— Same as Figure 3a

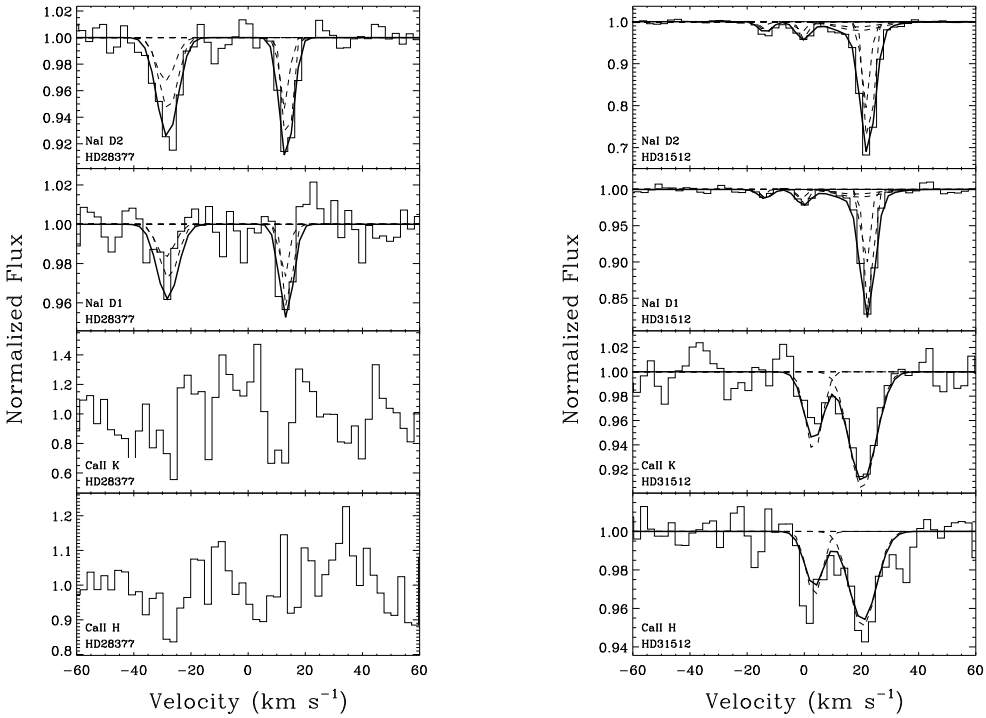

Fig. 3h.— Same as Figure 3a

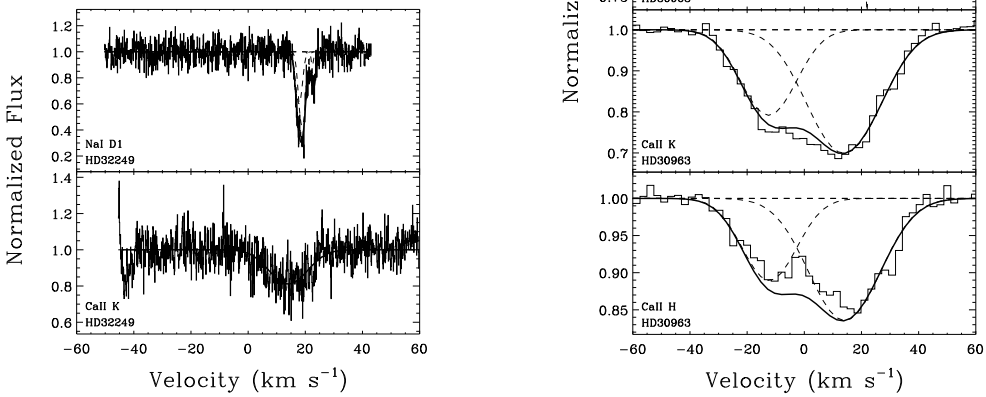

Fig. 3i.— Same as Figure 3a

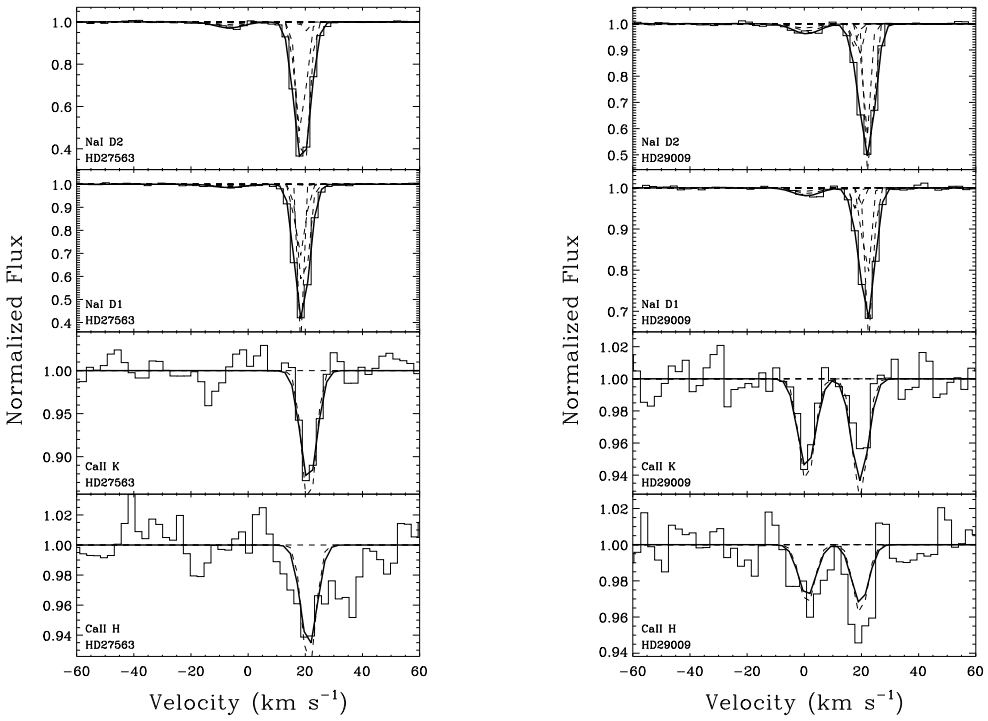

Fig. 3j.— Same as Figure 3a

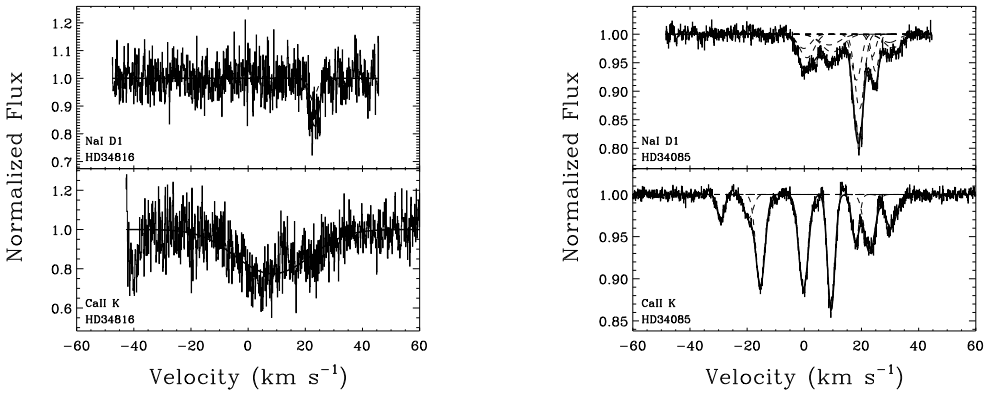

Fig. 3k.— Same as Figure 3a

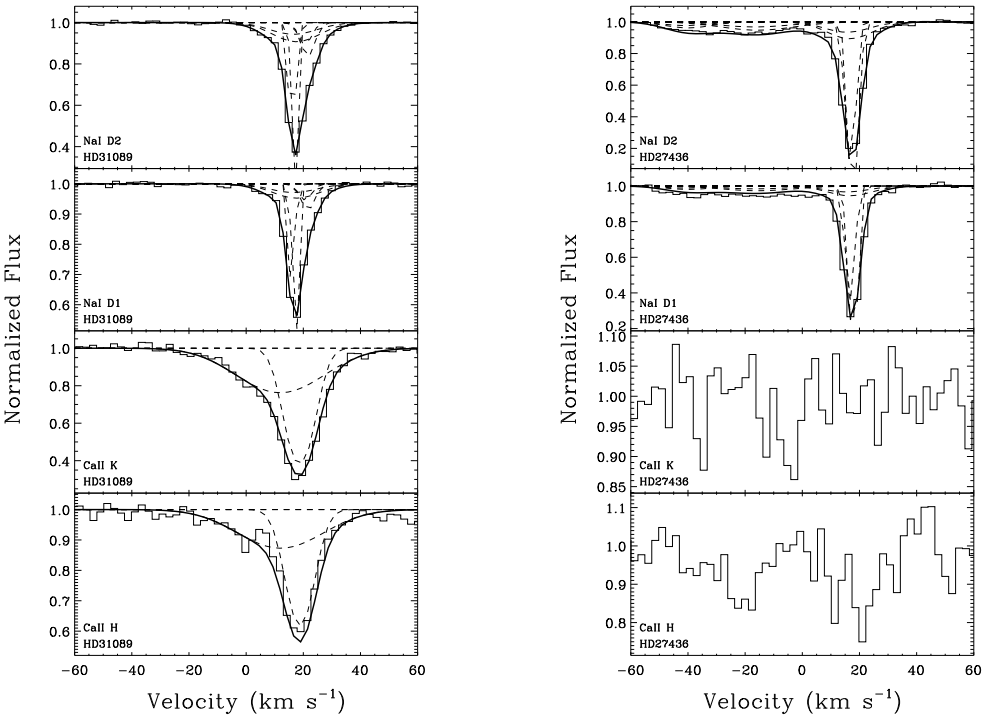

Fig. 3l.— Same as Figure 3a

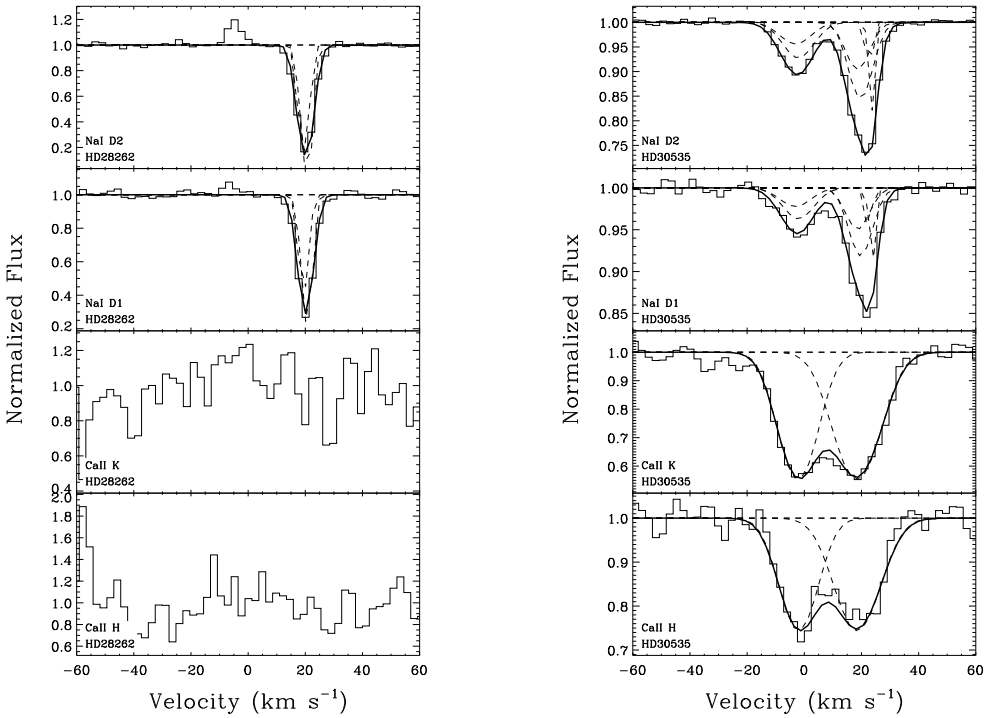

Fig. 3m.— Same as Figure 3a

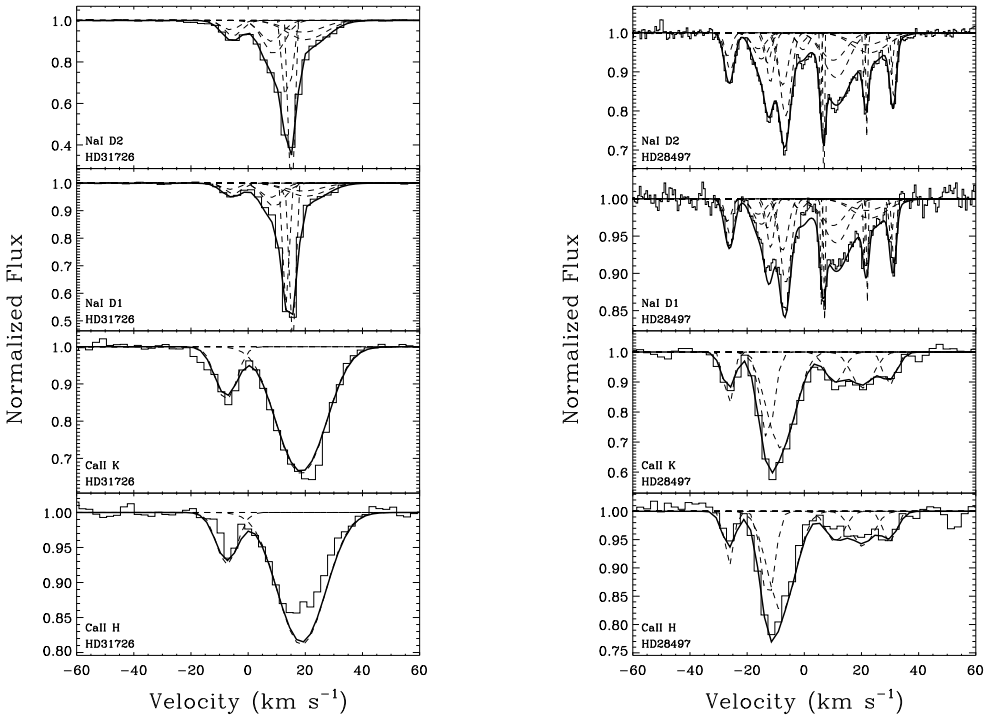

Fig. 3n.— Same as Figure 3a

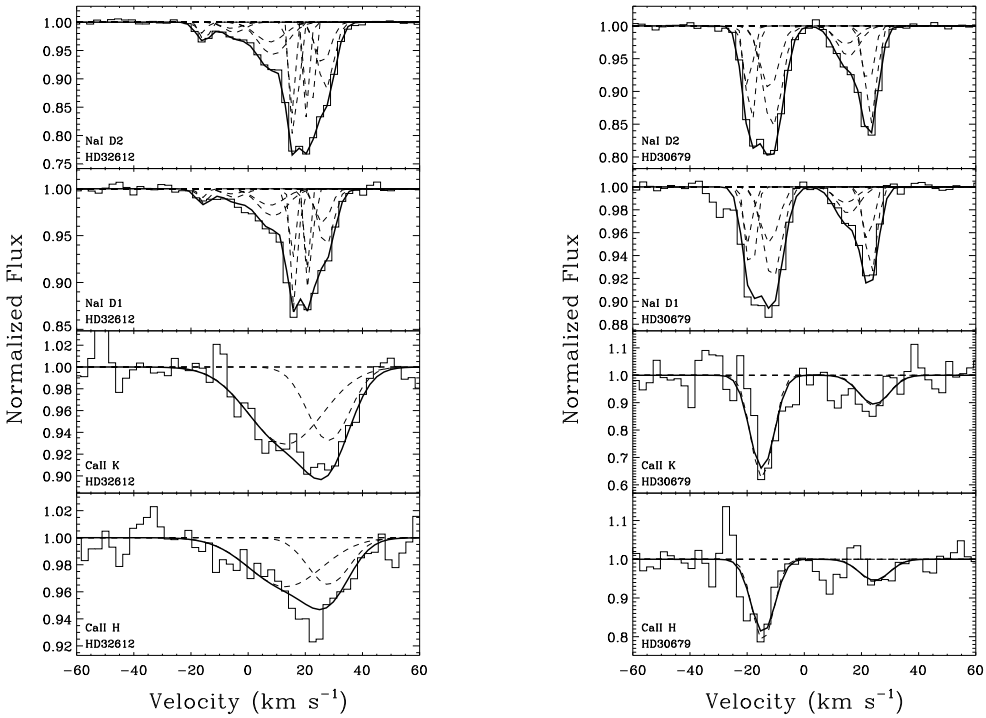

Fig. 3o.— Same as Figure 3a

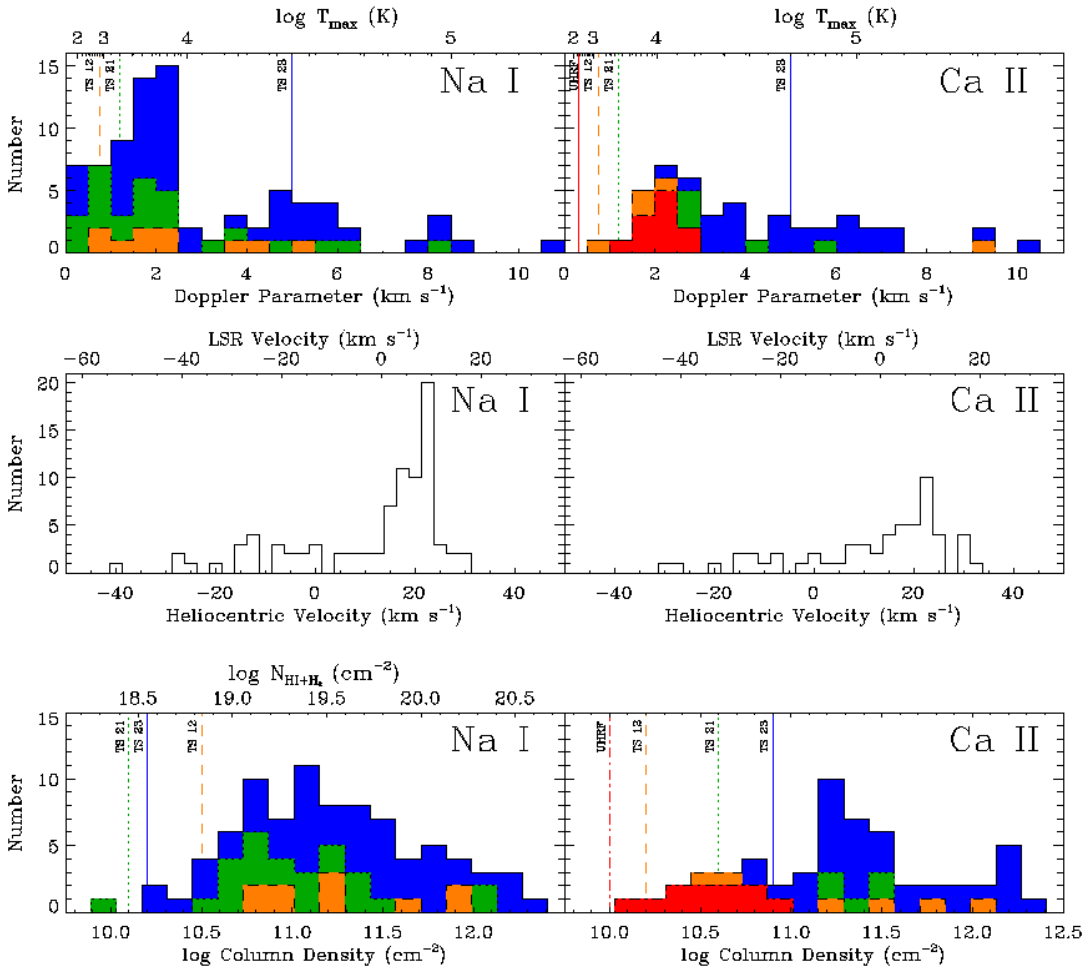

Fig. 4.— See caption on next page.

Fig. 4.— Distribution of ISM absorption fit parameters for both Na I and Ca II: Doppler parameter, or line width, (b) at the top; radial velocity (v) in the middle; and column density (N) at the bottom. The line width and column density distributions are color coded to differentiate between the various spectrographs used and their different resolving powers. The Doppler parameter distribution includes the spectral resolution limits of the various instruments. In addition, the top axis of the Doppler parameter distribution is a conversion of the line width into a maximum temperature, assuming no nonthermal, or turbulent, broadening. The Na I lines are consistently narrower than the Ca II lines, despite the lower atomic weight of sodium and larger sensitivity to thermal broadening. The velocity distribution is consistent between Na I and Ca II, and shows a preponderance of absorption at $\sim$20 km s^{-1}. The velocity distribution is not color coded due to the lack of any radial velocity bias induced by the differing spectral resolution. The column density distribution is shown together with an estimate of the sensitivity of each instrument. While dependent on spectral resolution, another significant factor is the efficiency of the spectrograph, which does not necessarily scale with the spectral resolution. The Ca II distribution shows a clear correlation with instrument, with the lowest column density measurements (N(Ca II) < 11) being made with the highest-resolution instrument (UHRF). The Ferlet et al. (1985) correlation between N(Na I) and N(H I+H_2) is used in the top axis of the Na I distribution.

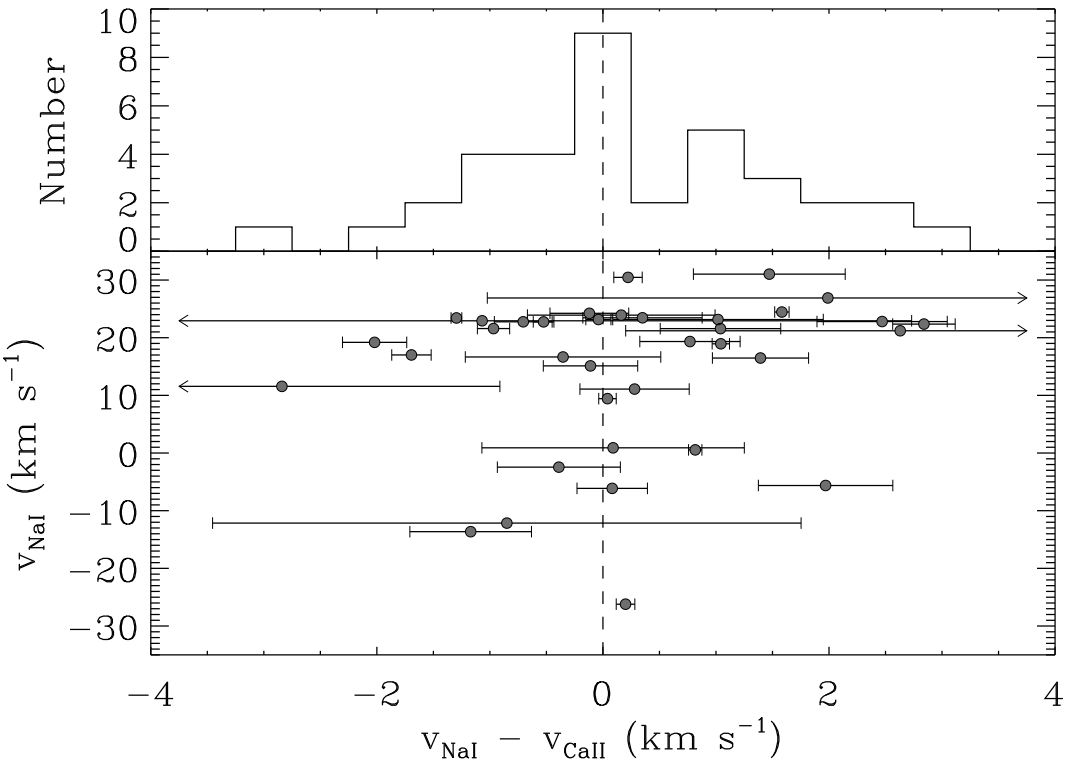

Fig. 5.— Comparison of central velocities between Na I and Ca II for those identified as paired components (i.e., $\Delta v < 3$ km s^{-1}). The distribution clearly peaks at zero although only 81% (29 out of 36) agree with zero within 3σ.

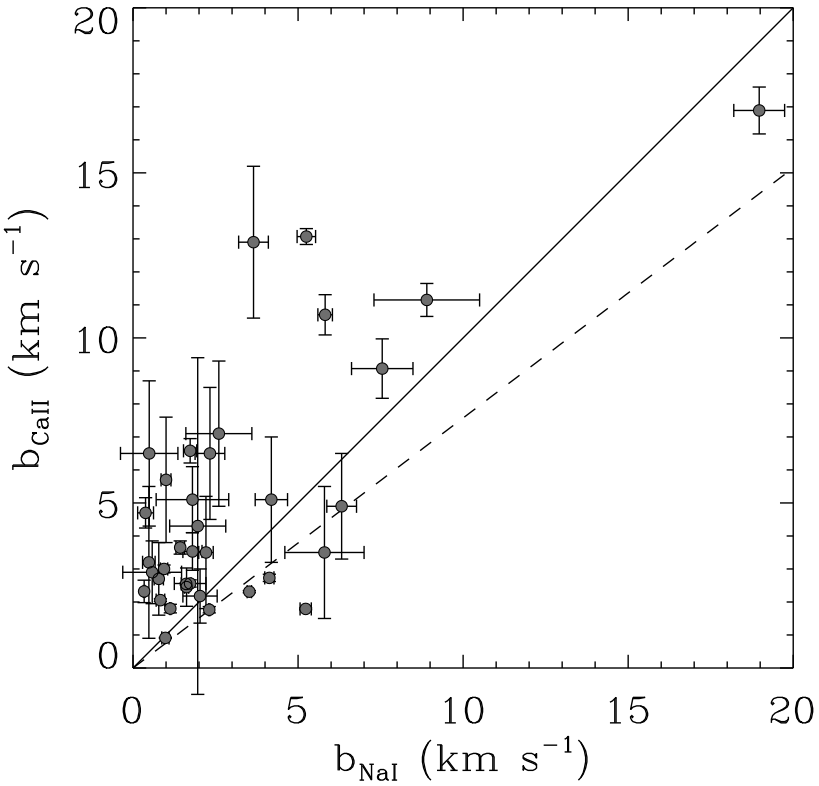

Fig. 6.— Comparison of Doppler parameters between Na I and Ca II for those identified as paired components (i.e., $\Delta v < 3$ km s^{-1}). The solid line indicates a purely turbulence-broadened profile, while the dashed line indicates a purely thermally broadened profile. Very few paired components fall between these two regimes, indicating that Na I and Ca II are not identically distributed. Instead, while possibly correlated, the two ions are largely segregated.

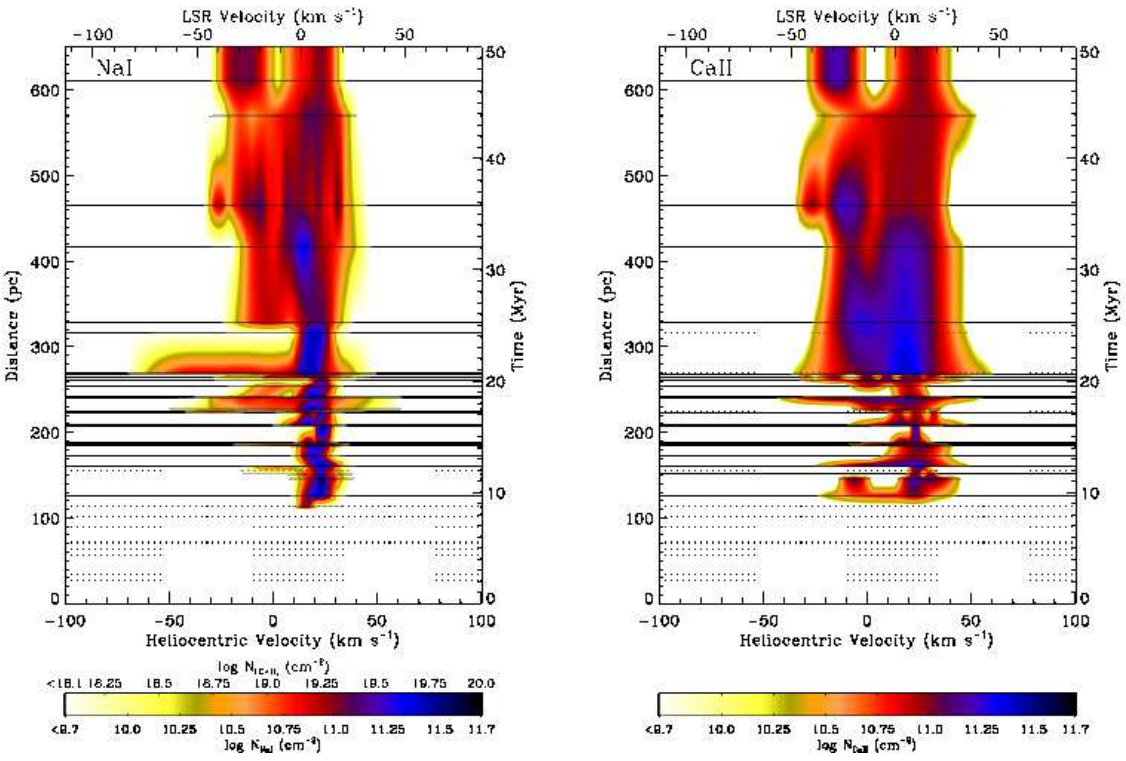

Fig. 7.— *left:* Apparent column density profile determined from the sodium data plotted at the distance to each star. The stellar distance is marked by black horizontal bars. Sight lines for which only upper limits were made are indicated by dotted lines. The distance axis is also displayed as a function of time, based on current values of the solar motion (Dehnen & Binney 1998). The Na I column density (N(Na I)) is converted to hydrogen column density (N(H I+H_2)) based on the correlation found by Ferlet et al. (1985). *right:* Same for the calcium data.

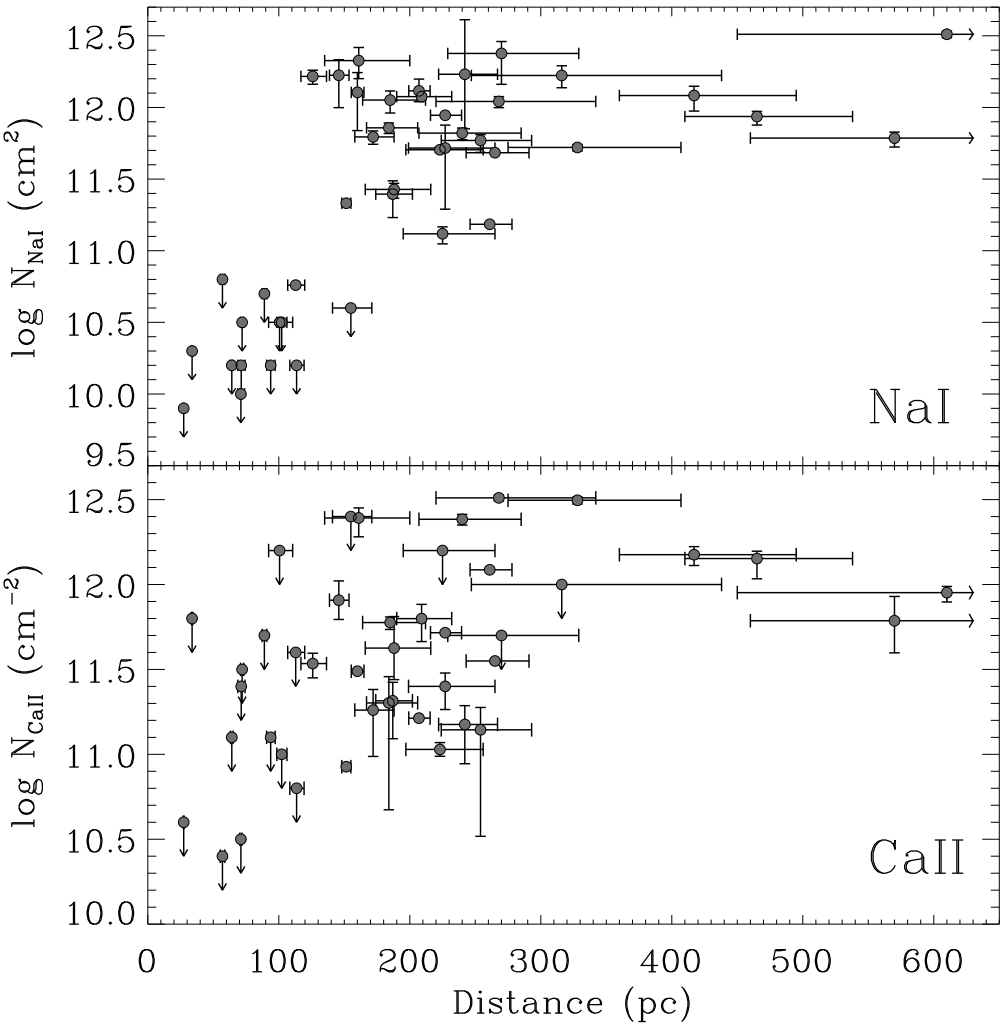

Fig. 8.— Total column density as a function of distance. Calcium (bottom panel) has significantly more scatter in the measurements of column density than the sodium data (top panel), likely due to the more dramatic effects of depletion on the calcium abundance in the gas phase. The first detection of cold, dense ISM lies at ∼120 pc, consistent with measurements of the Local Bubble boundary made by Lallement et al. (2003). Distances and errors are from the new analysis of *Hipparcos* parallax measurements (van Leeuwen 2007). Data are shown for 43 stars between ∼25 and ∼600 pc, with a median distance between stars of 5 pc. A dozen ISM absorption measurements inside the Local Bubble resulted in column density upper limits.

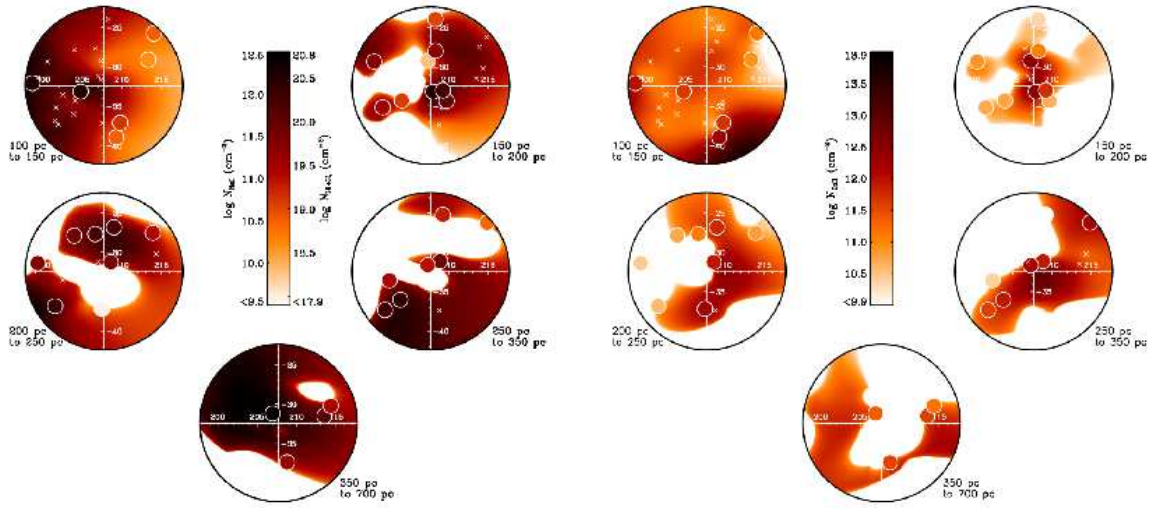

Fig. 9.— *left:* Spatial maps of sodium column density measurements in successive distance bins. The field of view has a radius of 10°. Circles indicate observed sight lines, and the color coding indicates the observed column density. The crosses are sight lines with constraining upper limits. The color coding throughout the field of view is an interpolation of the observed sight lines using a minimum curvature surface. Subsequent distance bins have previous column density maps subtracted, and so provide a contour map of ISM in each distance bin. The physical distances of 10° at the mean distance of each bin, from the nearest bin to the farthest, are 22.0 pc, 30.0 pc, 39.7 pc, 52.9 pc, and 92.6 pc, respectively. *right:* Same for the calcium data. While gross similarities exist between the ions, there are also significant differences, further emphasizing that these two ions are not spatially coincident.

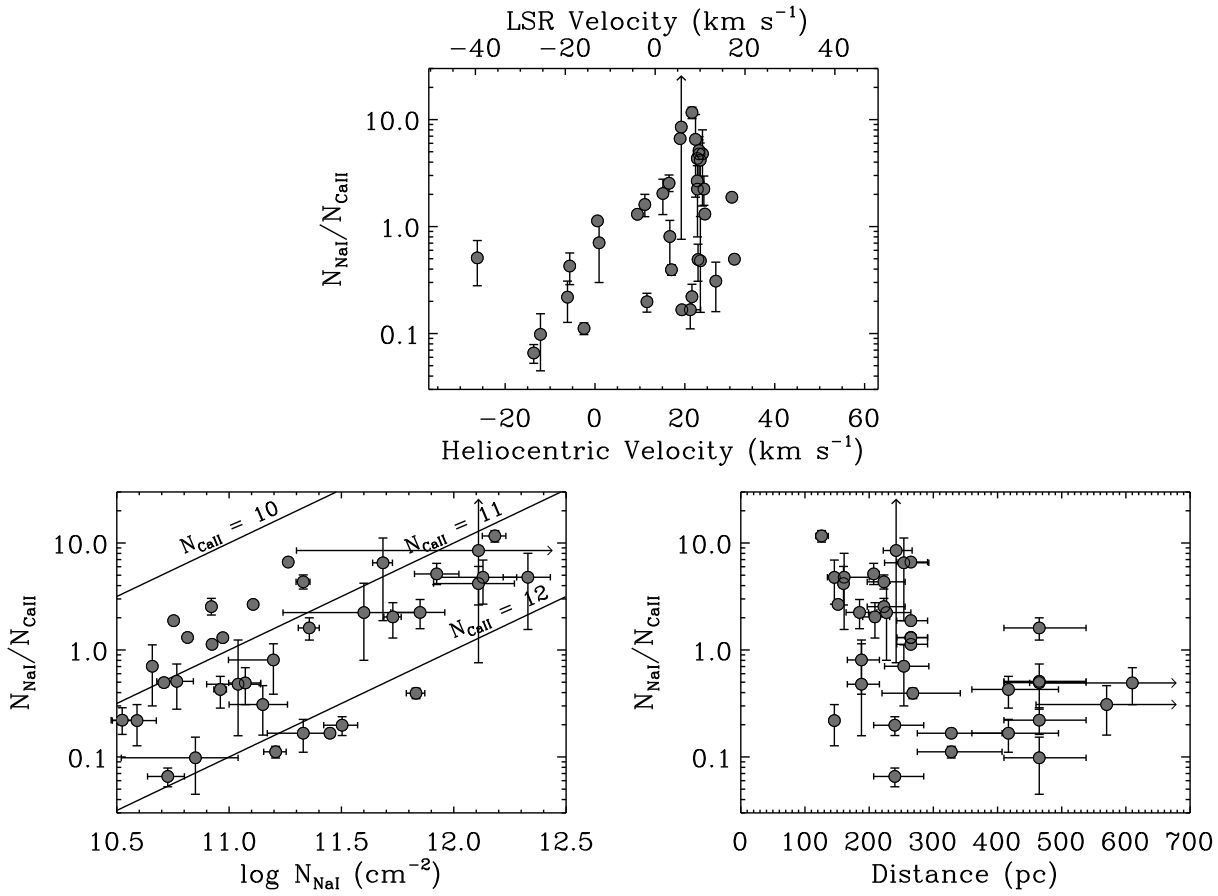

Fig. 10.— Measurements of the column density ratio between Na I and Ca II for those identified as paired components (i.e., $\Delta v < 3$ km s^{-1}). The top plot is the canonical Routly-Spitzer Effect, showing a large spread in velocity for components with small Na I/Ca II column density ratios, whereas those with high ratios have a small variation in velocity. The bottom left shows the column density ratio as a function of Na I column density. The solid lines indicate lines of constant Ca II column density ($\log N_{\rm CaII} = 10$, 11, 12). The correlation likely indicates the increase in calcium depletion in the densest ISM clouds. The bottom right shows the column density ratio as a function of stellar distance. The largest ratios are confined to the Local Bubble boundary region beyond ∼120 pc.

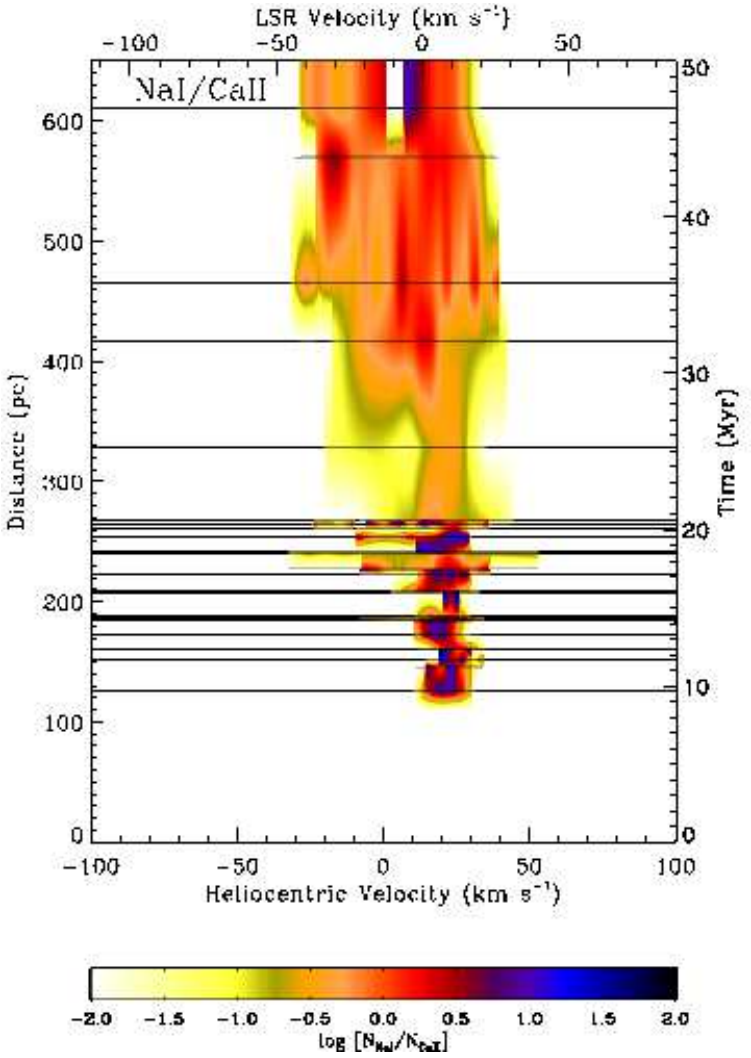

Fig. 11.— The Na I/Ca II column density ratio based on the apparent column density profiles shown in Figure 7. The high column density ratios are confined to the nearest sight lines and have a very narrow spread in velocity (i.e., the Routly-Spitzer Effect).

Table 1. Stellar Parameters for Targets along the Past Solar Trajectory[a]

HD #	Other Name	Spectral Type	m_V (mag)	v_R (km s^{-1})	$v \sin i$ (km s^{-1})	l (◦)	b (◦)	Distance[b] (pc)	$\Delta\theta$[c] (◦)
33111	β Eri	A3III	2.8	–9.2	195	205.34	–25.32	$27.40^{+0.32}_{-0.31}$	7.38
30743	HR1545	F5V	6.3	–3.0	7.0[d]	212.08	–33.12	$33.81^{+0.57}_{-0.55}$	3.75
33904	μ Lep	B9IV	3.3	27.7	18	217.25	–28.91	$57.0^{+1.8}_{-1.7}$	8.92
27861	ξ Eri	A2V	5.2	–11.0	179	197.82	–34.30	$64.1^{+1.0}_{-1.0}$	8.46
33802	ι Lep	B8V	4.5	25.0	190	212.67	–27.32	$71.07^{+0.82}_{-0.80}$	6.67
29573	HR1483	A0V	5.0	6.5	27	208.96	–34.85	$71.3^{+2.9}_{-2.6}$	2.66
31109	ω Eri	A9IV	4.4	–6.0	186	203.75	–28.78	$72.0^{+1.3}_{-1.2}$	4.97
32045	S Eri	F0V	4.8	–8.9	212	211.94	–30.34	$89.0^{+1.9}_{-1.8}$	4.17
30127	HR1513	A1V	5.5	5.0	195	216.99	–36.20	$93.8^{+3.4}_{-3.1}$	8.55
27925	HIP20521	A9IV/V	8.0			209.24	–38.96	$100.6^{+10.0}_{-8.4}$	6.67
34863	ν Lep	B7V	5.3	16.0	285	214.00	–25.79	$102.2^{+4.0}_{-3.7}$	8.61
28763	HR1438	A3V	6.3	–11.9[e]	102	209.75	–37.13	$112.9^{+6.9}_{-6.1}$	5.01
32996	HR1661	B9.5/A0IV	6.0	25.8[e]	26	213.32	–29.10	$113.6^{+5.7}_{-5.2}$	5.85
29554	HIP21640	B9	7.7			204.73	–33.15	$125.9^{+10.5}_{-9.0}$	2.60
28843	DZ Eri	B9III	5.8	18.4		198.62	–32.10	$145.8^{+7.8}_{-7.1}$	7.68
34503	τ Ori	B5III	3.6	20.1	40	208.28	–23.96	$151.5^{+3.5}_{-3.4}$	8.47
31625	HIP23011	A5	6.9	27.7	77	207.34	–29.25	155^{+16}_{-14}	3.18
30211	μ Eri	B5IV	4.0	8.5	150	200.53	–29.34	$160.0^{+5.0}_{-4.7}$	6.87
30050	RZ Eri	A	7.9	32.0	11[g]	208.00	–33.16	161^{+39}_{-26}	0.79
29851	HIP21837	A2IV/V	6.7			209.70	–34.37	172^{+16}_{-14}	2.57
28208	HIP20747	B9	7.3			201.61	–35.18	184^{+22}_{-17}	5.77
30332	HIP22169	B9	7.7			209.25	–33.00	185^{+27}_{-21}	1.43
28980	HIP21258	A0	6.6			204.05	–34.31	187^{+15}_{-13}	3.59
32468	HIP23493	A0	6.8			208.30	–28.00	188^{+28}_{-22}	4.44
29248	ν Eri	B2III	3.9	14.9	20	199.31	–31.38	$207.0^{+8.5}_{-7.8}$	7.20
33224	HR1671	B8V	5.8	27.0	155	208.95	–26.83	209^{+23}_{-19}	5.68
33949	κ Lep	B7V	4.4	18.0	120	213.88	–27.55	223^{+33}_{-26}	7.23
28377	HIP20849	A9IV	7.5			207.45	–37.20	225^{+40}_{-30}	4.79
32249	ψ Eri	B3V	4.8	25.4	30	206.59	–27.69	227^{+13}_{-11}	4.82
31512	62 Eri	B6V	5.5	24.0	80	203.93	–27.88	227^{+38}_{-28}	5.58
30963	HIP22588	B9	7.3			208.57	–31.24	240^{+45}_{-33}	1.38

Table 1—Continued

HD #	Other Name	Spectral Type	m_V (mag)	v_R (km s^{-1})	$v \sin i$ (km s^{-1})	l (◦)	b (◦)	Distance[b] (pc)	$\Delta\theta$[c] (◦)
27563	EM Eri	B5III	5.8	11.2	35	201.50	–36.83	242^{+25}_{-20}	6.75
29009	EH Eri	B9	5.7	1.7	55	202.47	–33.55	254^{+39}_{-30}	4.53
34816	λ Lep	B0.5IV	4.3	20.2	25	214.83	–26.24	261^{+17}_{-15}	8.75
34085	β Ori	B8I	0.1	20.7	40	209.24	–25.25	265^{+26}_{-22}	7.29
31089	HIP22669	B9V	7.8			208.90	–31.12	268^{+74}_{-48}	1.64
27436	HIP20179	A0	7.0			201.90	–37.34	270^{+59}_{-41}	6.85
28262	HIP20787	A0	8.6			203.85	–36.03	316^{+122}_{-69}	4.82
30535	HIP22304	A0	7.2			207.32	–31.65	328^{+79}_{-53}	0.83
31726	HR1595	B2V	6.1	11.4	5	213.50	–31.51	417^{+78}_{-57}	5.00
28497	DU Eri	B2V	5.6	22.0	295	208.78	–37.40	465^{+73}_{-55}	5.07
32612	HR1640	B2IV	6.4	16.0	65	214.33	–30.21	570^{+170}_{-110}	6.08
30679	HIP22406	A2	7.7			206.93	–31.19	610^{+330}_{-160}	1.38

[a]All values from SIMBAD unless otherwise noted.

[b]Distances calculated from *Hipparcos* parallaxes.

[c]Angular distance from direction of the past solar trajectory, $l = 207.70°$ and $b = -32.41°$ (Dehnen & Binney 1998).

[d]Nordström et al. (2004)

[e]Grenier et al. (1999)

[f]Shorlin et al. (2002)

[g]Stawikowski & Glebocki (1994)

Table 2. Observational Parameters for Stars along the Past Solar Trajectory

HD #	Other Name	Date	Telescope[a]	Instrument[b]	Ion	$v_{\rm atm}$ km s^{-1}	Exposure (s)	S/N
33111	β Eri	2003 Dec 3	McD2.7	TS12	Ca II		4800	27
33111	β Eri	2004 Oct 19	McD2.7	TS21	Na I	+21.2	1200	385
33111	β Eri	2004 Dec 1	McD2.7	TS23	Ca II, Na I	+2.7	300	52, 465
33111	β Eri	2005 Feb 27	AAT3.9	UHRF	Na I	–29.7	1200	82
33111	β Eri	2005 Feb 28	AAT3.9	UHRF	Ca II		1200	42
30743	HR1545	2005 Feb 14	McD2.7	TS21	Na I	–28.5	1200	46
30743	HR1545	2005 Feb 14	McD2.7	TS21	Ca II		2400	13
33904	μ Lep	2003 Oct 5	McD2.7	TS12	Ca II		3600	17
33904	μ Lep	2003 Dec 2	McD2.7	TS12	Na I	+3.9	3600	30
33904	μ Lep	2004 Oct 19	McD2.7	TS21	Ca II		1200	117
33904	μ Lep	2005 Oct 17	AAT3.9	UHRF	Ca II		2400	50
27861	ξ Eri	2005 Mar 16	McD2.7	TS21	Ca II		1800	49
27861	ξ Eri	2005 Mar 16	McD2.7	TS21	Na I	–26.6	1200	72
33802	ι Lep	2005 Jan 28	McD2.7	TS12	Ca II		4800	15
33802	ι Lep	2005 Feb 14	McD2.7	TS21	Na I	–27.4	1200	108
33802	ι Lep	2005 Feb 14	McD2.7	TS21	Ca II		1200	72
33802	ι Lep	2005 Feb 28	AAT3.9	UHRF	Ca II		1800	37
29573	HR1483	2003 Oct 2	McD2.7	TS12	Ca II		3600	4
29573	HR1483	2004 Oct 20	McD2.7	TS21	Na I	+19.2	1200	114
29573	HR1483	2004 Oct 20	McD2.7	TS21	Ca II		1200	42
31109	ω Eri	2004 Dec 1	McD2.7	TS23	Ca II, Na I	+0.7	900	23, 438
32045	S Eri	2004 Oct 20	McD2.7	TS21	Ca II		1200	54
32045	S Eri	2004 Oct 20	McD2.7	TS21	Na I	+21.1	600	86
30127	HR1513	2004 Oct 20	McD2.7	TS21	Ca II		1800	37
30127	HR1513	2004 Oct 20	McD2.7	TS21	Na I	+20.3	1800	109
27925	HIP20521	2004 Dec 6	McD2.7	TS23	Ca II, Na I	–4.9	1800	6, 83
34863	ν Lep	2005 Mar 16	McD2.7	TS21	Na I	–29.3	1200	56
34863	ν Lep	2005 Mar 16	McD2.7	TS21	Ca II		1800	47
28763	HR1438	2004 Oct 20	McD2.7	TS21	Ca II		1800	24
28763	HR1438	2004 Oct 20	McD2.7	TS21	Na I	+18.7	1800	78
32996	HR1661	2004 Dec 2	McD2.7	TS23	Ca II, Na I	+2.5	1800	92, 315

Table 2—Continued

HD #	Other Name	Date	Telescope[a]	Instrument[b]	Ion	$v_{\rm atm}$ km s^{-1}	Exposure (s)	S/N
29554	HIP21640	2004 Nov 30	McD2.7	TS23	Ca II, Na I	–0.3	1800	60, 206
28843	DZ Eri	2005 Mar 14	McD2.7	TS21	Ca II		2700	36
28843	DZ Eri	2005 Mar 14	McD2.7	TS21	Na I	–27.2	1800	32
34503	τ Ori	2003 Dec 3	McD2.7	TS12	Ca II		4800	38
34503	τ Ori	2004 Oct 19	McD2.7	TS21	Na I	+22.3	1200	265
31625	HIP23011	2004 Dec 6	McD2.7	TS23	Ca II, Na I	–1.1	1800	4, 113
30211	μ Eri	2003 Dec 3	McD2.7	TS12	Ca II		3600	18
30211	μ Eri	2004 Oct 18	McD2.7	TS21	Na I	+19.3	1200	131
30211	μ Eri	2004 Oct 18	McD2.7	TS21	Ca II		600	41
30211	μ Eri	2004 Nov 30	McD2.7	TS23	Ca II, Na I	+0.1	900	184, 522
30050	RZ Eri	2004 Dec 1	McD2.7	TS23	Ca II, Na I	–0.0	1800	16, 156
29851	HIP21837	2004 Dec 2	McD2.7	TS23	Ca II, Na I	–0.7	1800	45, 238
28208	HIP20747	2004 Dec 6	McD2.7	TS23	Ca II, Na I	–5.1	1800	15, 96
30332	HIP22169	2004 Nov 30	McD2.7	TS23	Ca II, Na I	+0.9	600	0, 3
30332	HIP22169	2004 Dec 1	McD2.7	TS23	Ca II, Na I	+0.4	1800	40, 136
28980	HIP21258	2004 Dec 2	McD2.7	TS23	Ca II, Na I	–2.0	1800	46, 181
32468	HIP23493	2005 Feb 14	McD2.7	TS21	Ca II		1800	21
32468	HIP23493	2005 Feb 14	McD2.7	TS21	Na I	–27.5	1200	28
29248	ν Eri	2003 Dec 1	McD2.7	TS12	Ca II		3600	36
29248	ν Eri	2003 Dec 2	McD2.7	TS12	Na I	–1.5	3600	25
33224	HR1671	2004 Nov 30	McD2.7	TS23	Ca II, Na I	+3.5	900	38, 186
33949	κ Lep	2004 Dec 3	McD2.7	TS23	Ca II, Na I	+2.8	1800	0, 7
33949	κ Lep	2005 Feb 14	McD2.7	TS21	Ca II		1200	68
33949	κ Lep	2005 Feb 14	McD2.7	TS21	Na I	–27.4	1200	93
33949	κ Lep	2005 Feb 27	AAT3.9	UHRF	Na I	–29.7	2400	30
33949	κ Lep	2005 Feb 28	AAT3.9	UHRF	Ca II		1800	37
28377	HIP20849	2004 Dec 6	McD2.7	TS23	Ca II, Na I	–4.5	1800	8, 101
32249	ψ Eri	2003 Dec 1	McD2.7	TS12	Ca II		4800	19
32249	ψ Eri	2003 Dec 2	McD2.7	TS12	Na I	+1.9	4800	19
32249	ψ Eri	2004 Nov 30	McD2.7	TS23	Ca II, Na I	+2.5	900	164, 398
31512	62 Eri	2004 Nov 30	McD2.7	TS23	Ca II, Na I	+1.7	900	71, 240

Table 2—Continued

HD #	Other Name	Date	Telescope[a]	Instrument[b]	Ion	$v_{\rm atm}$ km s^{-1}	Exposure (s)	S/N
30963	HIP22588	2004 Nov 30	McD2.7	TS23	Ca II, Na I	+1.5	1800	66, 241
27563	EM Eri	2004 Dec 1	McD2.7	TS23	Ca II, Na I	–3.2	900	74, 273
29009	EH Eri	2004 Dec 1	McD2.7	TS23	Ca II, Na I	–1.6	900	71, 275
34816	λ Lep	2003 Dec 1	McD2.7	TS12	Ca II		4800	16
34816	λ Lep	2003 Dec 2	McD2.7	TS12	Na I	+4.6	4800	25
34085	β Ori	2003 Dec 1	McD2.7	TS12	Ca II		2400	119
34085	β Ori	2003 Dec 2	McD2.7	TS12	Na I	+3.7	2400	143
34085	β Ori	2004 Dec 2	McD2.7	TS23	Ca II, Na I	+3.3	10	105, 431
34085	β Ori	2005 Feb 27	AAT3.9	UHRF	Na I	–29.7	900	316
34085	β Ori	2005 Feb 28	AAT3.9	UHRF	Ca II		900	246
34085	β Ori	2005 Mar 22	McD2.7	TS12	Ca II		2400	129
34085	β Ori	2006 Feb 17	McD2.7	TS21	Ca II		1200	107
34085	β Ori	2006 Feb 17	McD2.7	TS21	Na I	–27.4	600	346
31089	HIP22669	2004 Dec 1	McD2.7	TS23	Ca II, Na I	+1.1	1800	41, 143
27436	HIP20179	2004 Dec 6	McD2.7	TS23	Ca II, Na I	–5.9	1800	15, 102
28262	HIP20787	2004 Dec 6	McD2.7	TS23	Ca II, Na I	–4.9	2700	9, 65
30535	HIP22304	2004 Dec 1	McD2.7	TS23	Ca II, Na I	+0.4	1800	29, 178
31726	HR1595	2004 Dec 1	McD2.7	TS23	Ca II, Na I	+2.0	1800	122, 301
28497	DU Eri	2004 Oct 19	McD2.7	TS21	Ca II		1200	52
28497	DU Eri	2004 Oct 19	McD2.7	TS21	Na I	+18.8	1200	98
28497	DU Eri	2004 Nov 30	McD2.7	TS23	Ca II, Na I	–1.2	900	70, 228
32612	HR1640	2004 Dec 2	McD2.7	TS23	Ca II, Na I	+2.3	1800	86, 284
30679	HIP22406	2004 Dec 2	McD2.7	TS23	Ca II, Na I	+0.1	1800	17, 190

[a]McD2.7: the Harlan J. Smith 2.7m Telescope at McDonald Observatory; AAT3.9: the Anglo-Australian 3.9m Telescope at the Anglo-Australian Observatory.

[b]TS12: Coudé double-pass Spectrometer (R ∼400,000); TS21: Cross-Dispersed Echelle Spectrometer (2D Coudé) Focus 1 (R ∼240,000); TS23: Cross-Dispersed Echelle Spectrometer (2D Coudé) Focus 3 (R ∼60,000); UHRF: Ultra-High-Resolution Facility (R ∼940,000).

Table 3. Ca II ISM Fit Parameters for Targets along the Past Solar Trajectory

HD #	Other Name	Component #	Instrument	v (km s^{-1})	b (km s^{-1})	$\log N$ (cm^{-2})	Component # of Pair in Na I
29554	HIP21640	1	TS23	7.8 ± 4.1	19.3 ± 4.5	$11.32^{+0.11}_{-0.12}$	
29554	HIP21640	2	TS23	22.548 ± 0.091	3.65 ± 0.20	$11.117^{+0.011}_{-0.011}$	2
28843	DZ Eri	1	TS21	–6.212 ± 0.21	2.90 ± 0.95	$11.25^{+0.13}_{-0.19}$	1
28843	DZ Eri	2	TS21	22.13 ± 0.93	2.7 ± 1.1	$11.451^{+0.073}_{-0.089}$	3
28843	DZ Eri	3	TS21	31.2 ± 2.4	5.6 ± 2.6	$11.5^{+0.3}_{-1.2}$	
34503	τ Ori	1	TS12	23.266 ± 0.091	1.80 ± 0.13	10.681 ±0.021	2
34503	τ Ori	2	TS12	30.23 ± 0.11	1.64 ± 0.14	10.562 ±0.028	
30211	μ Eri	1	TS12	24.715 ± 0.037	2.055 ± 0.041	11.489 ±0.0094	1
30050	RZ Eri	1	TS23	11.0 ± 2.2	14.5 ± 3.0	$12.305^{+0.061}_{-0.071}$	
30050	RZ Eri	2	TS23	23.75 ± 0.83	3.5 ± 1.7	$11.65^{+0.21}_{-0.44}$	1
29851	HIP21837	1	TS23	23.36 ± 0.36	6.2 ± 3.9	$11.26^{+0.14}_{-0.20}$	
28208	HIP20747	1	TS23	23.8 ± 1.6	7.3 ± 1.1	$11.30^{+0.19}_{-0.33}$	
30332	HIP22169	1	TS23	8.4 ± 1.5	6.01 ± 0.68	$11.448^{+0.032}_{-0.033}$	
30332	HIP22169	2	TS23	24.35 ± 0.22	6.5 ± 2.0	$11.499^{+0.058}_{-0.067}$	2
28980	HIP21258	1	TS23	13.15 ± 0.95	10.2 ± 2.6	$11.31^{+0.12}_{-0.17}$	
32468	HIP23493	1	TS21	17.01 ± 0.86	2.548 ± 0.032	$11.29^{+0.15}_{-0.20}$	1
32468	HIP23493	2	TS21	23.10 ± 0.47	4.3 ± 5.1	11.36 ±0.41	2
29248	ν Eri	1	TS12	23.190 ± 0.015	0.912 ± 0.016	11.213 ±0.0057	1
33224	HR1671	1	TS23	15.22 ± 0.40	5.7 ± 1.9	$11.42^{+0.13}_{-0.19}$	1
33224	HR1671	2	TS23	20.6 ± 1.4	11.7 ± 1.6	$11.57^{+0.13}_{-0.14}$	
33949	κ Lep	1	UHRF	15.08 ± 0.42	2.45 ± 0.58	10.516 ±0.076	1
33949	κ Lep	2	UHRF	23.46 ± 0.25	2.32 ± 0.34	10.693 ±0.058	2
33949	κ Lep	3	UHRF	32.00 ± 0.34	1.38 ± 0.67	10.391 ±0.081	
32249	ψ Eri	1	TS12	14.03 ± 0.15	9.19 ± 0.22	11.715 ±0.0091	
31512	62 Eri	1	TS23	2.9 ± 1.2	3.82 ± 0.90	$10.87^{+0.10}_{-0.12}$	
31512	62 Eri	2	TS23	20.33 ± 0.45	6.5 ± 2.2	$11.25^{+0.12}_{-0.16}$	4
30963	HIP22588	1	TS23	–12.47 ± 0.092	13.07 ± 0.24	$11.909^{+0.029}_{-0.031}$	2
30963	HIP22588	2	TS23	14.4 ± 1.9	16.89 ± 0.71	$12.206^{+0.042}_{-0.047}$	3
27563	EM Eri	1	TS23	21.21 ± 0.18	3.2 ± 2.3	$11.18^{+0.13}_{-0.18}$	2
29009	EH Eri	1	TS23	0.81 ± 0.59	3.5 ± 2.0	$10.81^{+0.20}_{-0.37}$	1
29009	EH Eri	2	TS23	19.52 ± 0.18	3.53 ± 0.57	$10.87^{+0.23}_{-0.53}$	3

Table 3—Continued

HD #	Other Name	Component #	Instrument	v (km s^{-1})	b (km s^{-1})	log N (cm^{-2})	Component # of Pair in Na I
34816	λ Lep	1	TS12	8.61 ± 0.21	17.65 ± 0.28	12.086 ±0.0062	
34085	β Ori	1	UHRF	–29.20 ± 0.061	1.645 ± 0.076	10.157 ±0.019	
34085	β Ori	2	UHRF	–19.48 ± 0.45	2.27 ± 0.37	10.241 ±0.089	
34085	β Ori	3	UHRF	–15.32 ± 0.071	2.201 ± 0.085	10.834 ±0.036	
34085	β Ori	4	UHRF	–0.271 ± 0.024	2.312 ± 0.032	10.871 ±0.0052	1
34085	β Ori	5	UHRF	9.389 ± 0.019	1.790 ± 0.026	10.857 ±0.0061	2
34085	β Ori	6	UHRF	17.898 ± 0.076	1.765 ± 0.095	10.441 ±0.021	3
34085	β Ori	7	UHRF	22.867 ± 0.060	2.56 ± 0.11	10.698 ±0.014	4
34085	β Ori	8	UHRF	30.238 ± 0.076	2.73 ± 0.11	10.479 ±0.015	5
31089	HIP22669	1	TS23	11.98 ± 0.57	20.3 ± 4.6	$12.180^{+0.017}_{-0.017}$	
31089	HIP22669	2	TS23	18.70 ± 0.17	6.58 ± 0.37	$12.236^{+0.026}_{-0.027}$	1
30535	HIP22304	1	TS23	–2.06 ± 0.19	9.07 ± 0.90	$12.159^{+0.021}_{-0.022}$	1
30535	HIP22304	2	TS23	18.56 ± 0.41	10.70 ± 0.61	$12.227^{+0.032}_{-0.034}$	2
31726	HR1595	1	TS23	–7.60 ± 0.57	5.1 ± 1.9	$11.33^{+0.12}_{-0.17}$	1
31726	HR1595	2	TS23	18.57 ± 0.78	11.15 ± 0.50	$12.108^{+0.055}_{-0.063}$	4
28497	DU Eri	1	TS23	–26.41 ± 0.019	2.18 ± 0.82	$11.06^{+0.15}_{-0.23}$	1
28497	DU Eri	2	TS23	–11.3 ± 2.6	5.1 ± 1.0	$11.858^{+0.045}_{-0.051}$	3
28497	DU Eri	3	TS23	–10.2 ± 4.9	3.10 ± 0.69	$11.27^{+0.26}_{-0.75}$	
28497	DU Eri	4	TS23	10.81 ± 0.20	4.9 ± 1.6	$11.151^{+0.086}_{-0.099}$	7
28497	DU Eri	5	TS23	20.53 ± 0.46	4.70 ± 0.46	$11.18^{+0.11}_{-0.12}$	8
28497	DU Eri	6	TS23	29.55 ± 0.67	3.00 ± 0.12	$11.015^{+0.039}_{-0.040}$	10
32612	HR1640	1	TS23	4.1 ± 9.7	13.4 ± 4.9	$11.19^{+0.29}_{-0.73}$	
32612	HR1640	2	TS23	24.9 ± 3.0	12.9 ± 2.3	$11.66^{+0.15}_{-0.21}$	6
30679	HIP22406	1	TS23	–14.5 ± 1.5	4.80 ± 0.43	$11.816^{+0.021}_{-0.022}$	
30679	HIP22406	2	TS23	24.0 ± 3.8	7.1 ± 2.2	$11.38^{+0.13}_{-0.18}$	4

Note. — This table only lists those sight lines with detected Ca II absorption. The upper limits for sight lines with no detected absorption are given in Table 4.

Table 4. Ca II ISM Fit Parameters Total Column Density Per Sight Line

HD #	Other Name	Components	Instrument	$\log N$ (cm^{-2})	Other References
33111	β Eri		UHRF	<10.6	1
30743	HR1545		TS21	<11.8	···
33904	μ Lep		UHRF	<10.4	···
27861	ξ Eri		TS21	<11.1	···
33802	ι Lep		TS21	<10.5	1
29573	HR1483		TS21	<11.4	2
31109	ω Eri		TS23	<11.5	···
32045	S Eri		TS21	<11.7	···
30127	HR1513		TS21	<11.1	···
27925	HIP20521		TS23	<12.2	···
34863	ν Lep		TS21	<11.0	1
28763	HR1438		TS21	<11.6	···
32996	HR1661		TS23	<10.8	···
29554	HIP21640	2	TS23	$11.534\ ^{+0.061}_{-0.084}$	···
28843	DZ Eri	3	TS21	11.91 ±0.11	···
34503	τ Ori	2	TS12	10.927 ±0.017	1
31625	HIP23011		TS23	<12.4	···
30211	μ Eri	1	TS12	11.489 ±0.0094	3
30050	RZ Eri	2	TS23	$12.39\ ^{+0.06}_{-0.11}$	···
29851	HIP21837	1	TS23	$11.26\ ^{+0.12}_{-0.27}$	···
28208	HIP20747	1	TS23	$11.30\ ^{+0.15}_{-0.63}$	···
30332	HIP22169	2	TS23	$11.775\ ^{+0.033}_{-0.041}$	···
28980	HIP21258	1	TS23	$11.31\ ^{+0.10}_{-0.22}$	···
32468	HIP23493	2	TS21	11.63 ±0.19	···
29248	ν Eri	1	TS12	11.213 ±0.0057	3,4,5,6,7
33224	HR1671	2	TS23	$11.80\ ^{+0.08}_{-0.14}$	···
33949	κ Lep	3	UHRF	11.028 ±0.040	1
28377	HIP20849		TS23	<12.2	···
32249	ψ Eri	1	TS12	11.715 ±0.0091	1,3
31512	62 Eri	2	TS23	$11.40\ ^{+0.08}_{-0.14}$	···
30963	HIP22588	2	TS23	$12.384\ ^{+0.029}_{-0.034}$	···

Table 4—Continued

HD #	Other Name	Components	Instrument	$\log N$ (cm^{-2})	Other References
27563	EM Eri	1	TS23	$11.18\ ^{+0.11}_{-0.23}$	3
29009	EH Eri	2	TS23	$11.14\ ^{+0.13}_{-0.63}$	···
34816	λ Lep	1	TS12	12.086 ±0.0062	1,8
34085	β Ori	8	UHRF	11.549 ±0.011	7,9,10,11
31089	HIP22669	2	TS23	$12.510\ ^{+0.015}_{-0.017}$	···
27436	HIP20179		TS23	<11.7	···
28262	HIP20787		TS23	<12.0	···
30535	HIP22304	2	TS23	$12.496\ ^{+0.019}_{-0.022}$	···
31726	HR1595	2	TS23	$12.175\ ^{+0.047}_{-0.064}$	3,12
28497	DU Eri	6	TS23	$12.15\ ^{+0.04}_{-0.12}$	3,7,13,14,15,
32612	HR1640	3	TS23	$11.79\ ^{+0.14}_{-0.19}$	12
30679	HIP22406	2	TS23	$11.952\ ^{+0.036}_{-0.055}$	···

References. — (1) Frisch et al. 1990; (2) Holweger et al. 1999; (3) Welsh et al. 2005; (4) Adams 1949; (5) Burbidge & Burbidge 1953; (6) Münch & Zirin 1961; (7) Hobbs 1984; (8) Habing 1969; (9) Hobbs 1974; (10) Beintema 1975; (11) Price et al. 2001; (12) Albert et al. 1993; (13) Shull et al. 1977; (14) Penprase 1993; (15) Blades et al. 1997.

Table 5. Na I ISM Fit Parameters for Targets along the Past Solar Trajectory

HD #	Other Name	Component #	Instrument	v (km s^{-1})	b (km s^{-1})	$\log N$ (cm^{-2})	Component # of Pair in Ca II
28763	HR1438	1	TS21	15.491 ± 0.050	1.302 ± 0.040	$10.759\ ^{+0.0041}_{-0.0042}$	
29554	HIP21640	1	TS23	18.639 ± 0.045	0.482 ± 0.057	$11.089\ ^{+0.028}_{-0.030}$	
29554	HIP21640	2	TS23	21.58 ± 0.11	1.43 ± 0.13	$12.183\ ^{+0.049}_{-0.056}$	2
28843	DZ Eri	1	TS21	–6.13 ± 0.23	0.58 ± 0.89	$10.590\ ^{+0.086}_{-0.11}$	1
28843	DZ Eri	2	TS21	23.08 ± 0.21	4.78 ± 0.96	$11.466\ ^{+0.079}_{-0.096}$	
28843	DZ Eri	3	TS21	23.148 ± 0.049	0.78 ± 0.14	$12.13\ ^{+0.15}_{-0.22}$	2
34503	τ Ori	1	TS21	14.783 ± 0.045	0.63 ± 0.37	$9.9560\ ^{+0.037}_{-0.040}$	
34503	τ Ori	2	TS21	22.741 ± 0.0067	1.130 ± 0.018	$11.107\ ^{+0.0058}_{-0.0059}$	1
34503	τ Ori	3	TS21	22.487 ± 0.035	5.95 ± 0.14	$10.889\ ^{+0.021}_{-0.022}$	
30211	μ Eri	1	TS21	23.419 ± 0.030	0.83 ± 0.13	$12.11\ ^{+0.16}_{-0.20}$	1
30050	RZ Eri	1	TS23	23.912 ± 0.024	2.21 ± 0.22	$12.33\ ^{+0.10}_{-0.11}$	2
29851	HIP21837	1	TS23	19.362 ± 0.051	1.53 ± 0.21	$11.794\ ^{+0.044}_{-0.049}$	
28208	HIP20747	1	TS23	20.603 ± 0.048	2.05 ± 0.21	$11.857\ ^{+0.035}_{-0.038}$	
30332	HIP22169	1	TS23	5.79 ± 0.50	8.3 ± 1.0	$11.134\ ^{+0.044}_{-0.049}$	
30332	HIP22169	2	TS23	24.23 ± 0.27	2.33 ± 0.45	$11.85\ ^{+0.11}_{-0.13}$	2
30332	HIP22169	3	TS23	27.49 ± 0.21	0.318 ± 0.093	$11.441\ ^{+0.060}_{-0.069}$	
28980	HIP21258	1	TS23	20.29 ± 0.14	1.91 ± 0.70	$11.40\ ^{+0.10}_{-0.14}$	
32468	HIP23493	1	TS21	16.657 ± 0.090	1.61 ± 0.15	$11.197\ ^{+0.019}_{-0.020}$	1
32468	HIP23493	2	TS21	23.45 ± 0.24	1.96 ± 0.85	$11.04\ ^{+0.10}_{-0.14}$	2
29248	ν Eri	1	TS12	23.15 ± 0.11	0.98 ± 0.11	11.924 ± 0.099	1
29248	ν Eri	2	TS12	25.06 ± 0.36	1.31 ± 0.24	11.67 ± 0.13	
33224	HR1671	1	TS23	15.11 ± 0.12	1.00 ± 0.15	$11.729\ ^{+0.037}_{-0.040}$	1
33224	HR1671	2	TS23	17.512 ± 0.067	4.84 ± 0.12	$11.815\ ^{+0.0033}_{-0.0033}$	
33949	κ Lep	1	TS21	16.474 ± 0.067	1.622 ± 0.064	$10.921\ ^{+0.015}_{-0.016}$	1
33949	κ Lep	2	TS21	22.755 ± 0.052	0.337 ± 0.025	$11.330\ ^{+0.030}_{-0.032}$	2
33949	κ Lep	3	TS21	23.772 ± 0.067	2.10 ± 0.13	$11.320\ ^{+0.029}_{-0.031}$	
28377	HIP20849	1	TS23	–28.11 ± 0.70	4.51 ± 0.36	$10.853\ ^{+0.093}_{-0.12}$	
28377	HIP20849	2	TS23	13.40 ± 0.46	2.30 ± 0.36	$10.777\ ^{+0.021}_{-0.022}$	
32249	ψ Eri	1	TS12	18.484 ± 0.017	1.541 ± 0.031	11.869 ±0.0052	
32249	ψ Eri	2	TS12	22.697 ± 0.045	0.861 ± 0.081	11.152 ±0.017	
31512	62 Eri	1	TS23	–13.45 ± 0.25	1.62 ± 0.80	$10.29\ ^{+0.11}_{-0.16}$	

Table 5—Continued

HD #	Other Name	Component #	Instrument	v (km s^{-1})	b (km s^{-1})	log N (cm^{-2})	Component # of Pair in Ca II
31512	62 Eri	2	TS23	–0.370 ± 0.25	2.43 ± 0.84	$10.462^{+0.055}_{-0.063}$	
31512	62 Eri	3	TS23	19.7 ± 1.3	8.41 ± 2.0	$10.90^{+0.15}_{-0.24}$	
31512	62 Eri	4	TS23	22.80 ± 0.36	0.49 ± 0.87	$11.60^{+0.26}_{-0.36}$	2
30963	HIP22588	1	TS23	–24.2 ± 1.8	1.5 ± 1.1	$10.268^{+0.050}_{-0.050}$	
30963	HIP22588	2	TS23	–13.64 ± 0.53	5.25 ± 0.28	$10.727^{+0.074}_{-0.090}$	1
30963	HIP22588	3	TS23	11.56 ± 0.33	18.97 ± 0.77	$11.503^{+0.069}_{-0.082}$	2
30963	HIP22588	4	TS23	21.411 ± 0.026	1.56 ± 0.16	$11.433^{+0.038}_{-0.041}$	
27563	EM Eri	1	TS23	–6.36 ± 0.51	5.8 ± 3.7	$10.54^{+0.14}_{-0.22}$	
27563	EM Eri	2	TS23	18.893 ± 0.094	2.53 ± 0.67	$11.59^{+0.27}_{-0.77}$	
27563	EM Eri	3	TS23	19.19 ± 0.22	0.48 ± 0.19	12.11 ±0.81	1
29009	EH Eri	1	TS23	0.9 ± 1.0	5.8 ± 1.2	$10.658^{+0.015}_{-0.016}$	1
29009	EH Eri	2	TS23	18.3 ± 1.0	1.49 ± 0.72	$10.76^{+0.25}_{-0.67}$	
29009	EH Eri	3	TS23	22.36 ± 0.21	1.80 ± 0.29	$11.685^{+0.042}_{-0.046}$	2
34816	λ Lep	1	TS12	23.208 ± 0.066	2.14 ± 0.11	11.184 ±0.016	
34085	β Ori	1	TS12	0.546 ± 0.054	3.524 ± 0.066	10.924 ±0.0095	4
34085	β Ori	2	TS12	9.429 ± 0.075	5.23 ± 0.17	10.972 ±0.011	5
34085	β Ori	3	TS12	18.941 ± 0.011	2.310 ± 0.019	11.263 ±0.0030	6
34085	β Ori	4	TS12	24.450 ± 0.021	1.73 ± 0.48	10.815 ±0.0099	7
34085	β Ori	5	TS12	30.46 ± 0.10	4.13 ± 0.14	10.753 ±0.011	8
31089	HIP22669	1	TS23	17.006 ± 0.039	1.73 ± 0.20	$11.832^{+0.039}_{-0.043}$	2
31089	HIP22669	2	TS23	17.4 ± 2.0	11.67 ± 0.30	$11.495^{+0.081}_{-0.10}$	
31089	HIP22669	3	TS23	22.58 ± 0.37	2.40 ± 0.75	$11.04^{+0.10}_{-0.13}$	
27436	HIP20179	1	TS23	–39.1 ± 2.9	11.8 ± 2.3	$11.201^{+0.093}_{-0.10}$	
27436	HIP20179	2	TS23	–12.3 ± 5.9	17. ± 10.	$11.46^{+0.38}_{-1.1}$	
27436	HIP20179	3	TS23	17.3 ± 7.5	11.0 ± 6.5	$11.30^{+0.36}_{-0.68}$	
27436	HIP20179	4	TS23	17.375 ± 0.055	2.39 ± 0.40	$12.24^{+0.10}_{-0.11}$	
28262	HIP20787	1	TS23	20.085 ± 0.048	2.37 ± 0.21	$12.223^{+0.074}_{-0.077}$	
30535	HIP22304	1	TS23	–2.45 ± 0.51	7.55 ± 0.93	$11.207^{+0.047}_{-0.053}$	1
30535	HIP22304	2	TS23	19.33 ± 0.17	5.82 ± 0.22	$11.449^{+0.0095}_{-0.0097}$	2
30535	HIP22304	3	TS23	23.22 ± 0.20	1.18 ± 0.37	$10.918^{+0.084}_{-0.10}$	
31726	HR1595	1	TS23	–5.63 ± 0.17	4.19 ± 0.49	$10.961^{+0.027}_{-0.029}$	1

Table 5—Continued

HD #	Other Name	Component #	Instrument	v (km s^{-1})	b (km s^{-1})	log N (cm^{-2})	Component # of Pair in Ca II
31726	HR1595	2	TS23	8.36 ± 0.64	5.09 ± 0.44	$11.400\ ^{+0.045}_{-0.050}$	
31726	HR1595	3	TS23	14.543 ± 0.012	1.04 ± 0.51	$11.82\ ^{+0.12}_{-0.17}$	
31726	HR1595	4	TS23	21.2 ± 2.3	8.9 ± 1.6	$11.33\ ^{+0.12}_{-0.16}$	2
28497	DU Eri	1	TS21	–26.21 ± 0.080	2.03 ± 0.52	$10.767\ ^{+0.074}_{-0.089}$	1
28497	DU Eri	2	TS21	–15.3 ± 1.6	3.75 ± 0.71	$10.74\ ^{+0.31}_{-0.50}$	
28497	DU Eri	3	TS21	–12.15 ± 0.13	1.8 ± 1.1	$10.85\ ^{+0.19}_{-0.33}$	2
28497	DU Eri	4	TS21	–6.909 ± 0.057	2.49 ± 0.51	$11.23\ ^{+0.11}_{-0.14}$	
28497	DU Eri	5	TS21	–1.2 ± 1.7	3.34 ± 0.55	$10.62\ ^{+0.16}_{-0.27}$	
28497	DU Eri	6	TS21	6.494 ± 0.054	0.21 ± 0.34	$10.66\ ^{+0.14}_{-0.22}$	
28497	DU Eri	7	TS21	11.09 ± 0.44	6.32 ± 0.45	$11.357\ ^{+0.044}_{-0.049}$	4
28497	DU Eri	8	TS21	21.57 ± 0.27	0.38 ± 0.24	$10.524\ ^{+0.044}_{-0.049}$	5
28497	DU Eri	9	TS21	23.5 ± 1.0	8.1 ± 1.2	$11.045\ ^{+0.062}_{-0.073}$	
28497	DU Eri	10	TS21	31.022 ± 0.045	0.94 ± 0.11	$10.710\ ^{+0.0070}_{-0.0071}$	6
32612	HR1640	1	TS23	–15.5 ± 1.1	2.4 ± 2.4	$10.42\ ^{+0.11}_{-0.11}$	
32612	HR1640	2	TS23	–4.1 ± 1.8	4.57 ± 0.97	$10.52\ ^{+0.10}_{-0.11}$	
32612	HR1640	3	TS23	8.01 ± 0.35	6.12 ± 0.86	$11.099\ ^{+0.064}_{-0.073}$	
32612	HR1640	4	TS23	15.86 ± 0.20	1.65 ± 0.44	$11.175\ ^{+0.068}_{-0.072}$	
32612	HR1640	5	TS23	21.14 ± 0.45	1.64 ± 0.46	$11.13\ ^{+0.13}_{-0.18}$	2
32612	HR1640	6	TS23	26.89 ± 0.28	3.65 ± 0.45	$11.15\ ^{+0.11}_{-0.15}$	
30679	HIP22406	1	TS23	–19.04 ± 0.16	2.4 ± 1.2	$11.059\ ^{+0.096}_{-0.12}$	
30679	HIP22406	2	TS23	–11.49 ± 0.37	4.54 ± 0.43	$11.335\ ^{+0.019}_{-0.019}$	
30679	HIP22406	3	TS23	15.37 ± 0.82	5.25 ± 0.31	$10.853\ ^{+0.030}_{-0.032}$	
30679	HIP22406	4	TS23	22.931 ± 0.022	2.6 ± 1.0	$11.072\ ^{+0.069}_{-0.074}$	2

Table 6. Na I ISM Fit Parameters Total Column Density Per Sight Line

HD #	Other Name	Number of Components	Instrument	$\log N$ (cm^{-2})	Other References
33111	β Eri		UHRF	<9.9	1
30743	HR1545		TS21	<10.3	···
33904	μ Lep		TS12	<10.8	2
27861	ξ Eri		TS21	<10.2	···
33802	ι Lep		TS21	<10.0	···
29573	HR1483		TS21	<10.2	3
31109	ω Eri		TS23	<10.5	···
32045	S Eri		TS21	<10.7	···
30127	HR1513		TS21	<10.2	···
27925	HIP20521		TS23	<10.5	···
34863	ν Lep		TS21	<10.5	···
28763	HR1438	1	TS21	$10.759\ ^{+0.0041}_{-0.0042}$	4,5
32996	HR1661		TS23	<10.2	···
29554	HIP21640	2	TS23	$12.216\ ^{+0.043}_{-0.055}$	···
28843	DZ Eri	3	TS21	$12.22\ ^{+0.11}_{-0.23}$	···
34503	τ Ori	3	TS21	$11.331\ ^{+0.0084}_{-0.0090}$	6
31625	HIP23011		TS23	<10.6	···
30211	μ Eri	1	TS21	$12.11\ ^{+0.14}_{-0.27}$	1,4,7
30050	RZ Eri	1	TS23	$12.326\ ^{+0.091}_{-0.13}$	···
29851	HIP21837	1	TS23	$11.794\ ^{+0.042}_{-0.052}$	5
28208	HIP20747	1	TS23	$11.857\ ^{+0.034}_{-0.040}$	···
30332	HIP22169	3	TS23	$12.051\ ^{+0.064}_{-0.090}$	···
28980	HIP21258	1	TS23	$11.395\ ^{+0.093}_{-0.16}$	···
32468	HIP23493	2	TS21	$11.428\ ^{+0.042}_{-0.062}$	···
29248	ν Eri	2	TS12	$12.116\ ^{+0.082}_{-0.076}$	4,8
33224	HR1671	2	TS23	$12.075\ ^{+0.016}_{-0.019}$	···
33949	κ Lep	3	TS21	$11.704\ ^{+0.017}_{-0.019}$	1
28377	HIP20849	2	TS23	$11.118\ ^{+0.048}_{-0.070}$	···
32249	ψ Eri	2	TS12	$11.945\ \pm0.0052$	4
31512	62 Eri	4	TS23	$11.72\ ^{+0.16}_{-0.43}$	7
30963	HIP22588	4	TS23	$11.820\ ^{+0.035}_{-0.046}$	···

Table 6—Continued

HD #	Other Name	Number of Components	Instrument	$\log N$ (cm^{-2})	Other References
27563	EM Eri	3	TS23	12.23 ±0.38	4
29009	EH Eri	3	TS23	$11.769\ ^{+0.040}_{-0.083}$	···
34816	λ Lep	1	TS12	11.184 ±0.016	8
34085	β Ori	5	TS12	11.684 ±0.0050	9,10,11
31089	HIP22669	3	TS23	$12.041\ ^{+0.034}_{-0.043}$	···
27436	HIP20179	4	TS23	$12.376\ ^{+0.083}_{-0.22}$	···
28262	HIP20787	1	TS23	$12.223\ ^{+0.068}_{-0.085}$	···
30535	HIP22304	3	TS23	$11.720\ ^{+0.020}_{-0.024}$	···
31726	HR1595	4	TS23	$12.083\ ^{+0.065}_{-0.11}$	4
28497	DU Eri	10	TS21	$11.936\ ^{+0.036}_{-0.059}$	4,5,8,12,13
32612	HR1640	6	TS23	$11.786\ ^{+0.042}_{-0.062}$	···
30679	HIP22406	4	TS23	$11.716\ ^{+0.027}_{-0.034}$	···

References. — (1) Welsh et al. 1994; (2) Welsh et al. 1991; (3) Holweger et al. 1999; (4) Welsh et al. 2005; (5) Penprase 1993; (6) Frisch et al. 1990; (7) Génova & Beckman 2003; (8) Hobbs 1978; (9) Hobbs 1969; (10) Hobbs 1974; (11) Price et al. 2001; (12) Shull et al. 1977; (13) Blades et al. 1997.

Table 7. Multiple-Resolution Fits

HD #	Other Name	Ion	Components	Instrument	$\log N$ (cm^{-2})
30211	μ Eri	Na I	1	TS21	$12.11\ ^{+0.14}_{-0.27}$
30211	μ Eri	Na I	2	TS23	$12.01\ ^{+0.14}_{-0.48}$
33949	κ Lep	Na I	3	TS21	$11.704\ ^{+0.017}_{-0.019}$
33949	κ Lep	Na I	3	UHRF	11.515 ± 0.028
32249	ψ Eri	Na I	2	TS12	11.945 ± 0.0052
32249	ψ Eri	Na I	3	TS23	$12.142\ ^{+0.050}_{-0.066}$
34085	β Ori	Na I	5	TS12	11.684 ± 0.0050
34085	β Ori	Na I	4	TS23	$11.671\ ^{+0.026}_{-0.035}$
34085	β Ori	Na I	4	UHRF	11.524 ± 0.0016
34085	β Ori	Na I	6	TS21	$11.664\ ^{+0.019}_{-0.027}$
28497	DU Eri	Na I	10	TS21	$11.936\ ^{+0.036}_{-0.060}$
28497	DU Eri	Na I	6	TS23	$11.948\ ^{+0.014}_{-0.016}$
30211	μ Eri	Ca II	1	TS12	11.489 ± 0.0094
30211	μ Eri	Ca II	2	TS21	11.73 ± 0.11
30211	μ Eri	Ca II	2	TS23	$11.738\ ^{+0.019}_{-0.021}$
32249	ψ Eri	Ca II	1	TS12	11.715 ± 0.0091
32249	ψ Eri	Ca II	3	TS23	$12.07\ ^{+0.10}_{-0.23}$
34085	β Ori	Ca II	5	TS12	11.507 ± 0.0030
34085	β Ori	Ca II	5	TS23	$11.48\ ^{+0.07}_{-0.13}$
34085	β Ori	Ca II	8	UHRF	11.549 ± 0.011
34085	β Ori	Ca II	7	TS12	11.517 ± 0.0042
28497	DU Eri	Ca II	5	TS21	$12.202\ ^{+0.034}_{-0.047}$
28497	DU Eri	Ca II	6	TS23	$12.152\ ^{+0.043}_{-0.12}$

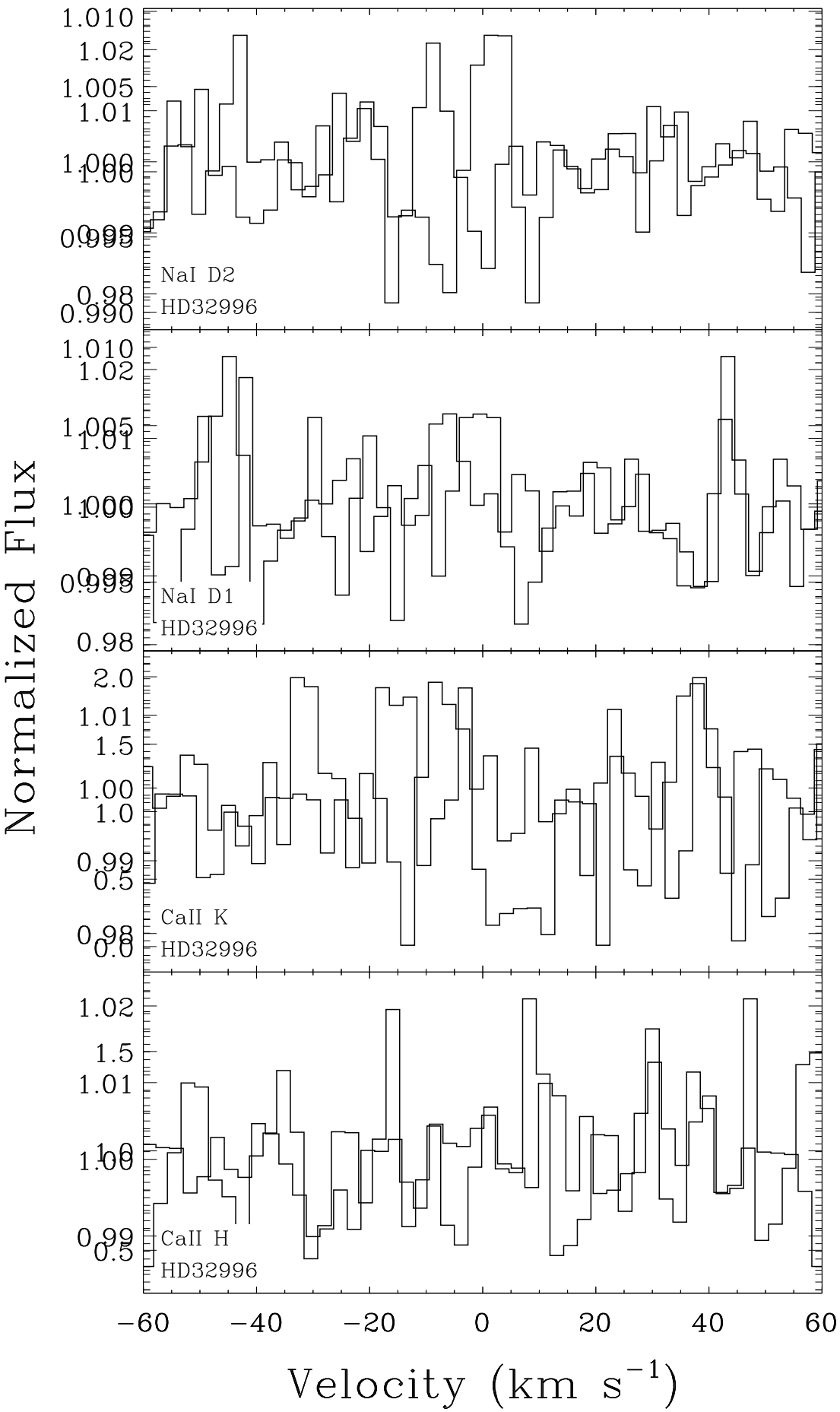
NaI D2
HD32996
NaI D1
HD32996
CaII K
HD32996
CaII H
HD32996
Normalized Flux
Velocity (km s^{-1})